

## A Data-driven Discovery of the Causal Connection between Galaxy and Black Hole Evolution

2 ZEHAO JIN (金泽灏) <sup>1, 2, 3</sup> MARIO PASQUATO <sup>3, 4, 5, 6, 7, \*</sup> BENJAMIN L. DAVIS <sup>1, 2, \*</sup> TRISTAN DELEU <sup>4, 8</sup>

3 YU LUO (罗煜) <sup>9, 10</sup> CHANGHYUN CHO <sup>1, 2</sup> PABLO LEMOS <sup>3, 4, 5</sup> LAURENCE PERREAULT-LEVASSEUR <sup>3, 4, 5, 11</sup>

4 YOSHUA BENGIO <sup>4, 8, 12, 13</sup> XI KANG (康熙) <sup>14, 10</sup> ANDREA VALERIO MACCIÒ <sup>1, 2, 15</sup> AND YASHAR HEZAVEH <sup>3, 4, 5, 11</sup>

5 <sup>1</sup> New York University Abu Dhabi, P.O. Box 129188, Abu Dhabi, United Arab Emirates

6 <sup>2</sup> Center for Astrophysics and Space Science (CASS), New York University Abu Dhabi, P.O. Box 129188, Abu Dhabi, UAE

7 <sup>3</sup> Montréal Institute for Astrophysical Data Analysis and Machine Learning (Ciela), Montréal, Canada

8 <sup>4</sup> Montréal Institute for Learning Algorithms (Mila), Quebec Artificial Intelligence Institute, 6666 Rue Saint-Urbain, Montréal, Canada

9 <sup>5</sup> Département de Physique, Université de Montréal, 1375 Avenue Thérèse-Lavoie-Roux, Montréal, Canada

10 <sup>6</sup> Dipartimento di Fisica e Astronomia, Università di Padova, Vicolo dell'Osservatorio 5, Padova, Italy

11 <sup>7</sup> Istituto di Astrofisica Spaziale e Fisica Cosmica (INAF IASF-MI), Via Alfonso Corti 12, I-20133, Milan, Italy

12 <sup>8</sup> Département d'Informatique et de Recherche Opérationnelle, Université de Montréal, 2920 Chemin de la Tour, Montréal, Canada

13 <sup>9</sup> Department of Physics, School of Physics and Electronics, Hunan Normal University, Changsha 410081, China

14 <sup>10</sup> Purple Mountain Observatory, 10 Yuan Hua Road, Nanjing 210034, China

15 <sup>11</sup> Center for Computational Astrophysics, Flatiron Institute, New York, NY, United States of America

16 <sup>12</sup> Canadian Institute for Advanced Research Artificial Intelligence Chair

17 <sup>13</sup> Canadian Institute for Advanced Research Senior Fellow

18 <sup>14</sup> Institute for Astronomy, Zhejiang University, Hangzhou 310027, China

19 <sup>15</sup> Max-Planck-Institut für Astronomie, Königstuhl 17, 69117 Heidelberg, Germany

20 (Received September 16, 2024)

21 Submitted to ApJ

## ABSTRACT

23 Correlations between galaxies and their supermassive black holes (SMBHs) have been observed, but  
24 the causal mechanisms remained unclear. The emerging field of causal inference now enables examining  
25 these relationships using observational data. This study, using advanced causal discovery techniques  
26 and a state-of-the-art dataset, reveals a causal link between galaxy properties and SMBH masses. In  
27 elliptical galaxies, bulge properties influence SMBH growth, while in spiral galaxies, SMBHs affect  
28 host galaxy properties, potentially through feedback in gas-rich environments. For spiral galaxies,  
29 SMBHs progressively quench star formation, whereas in elliptical galaxies, quenching is complete, and  
30 the causal connection has reversed. These findings support theoretical models of active galactic nuclei  
31 feedback regulating galaxy evolution and suggest further exploration of causal links in astrophysical  
32 and cosmological scaling relations.

33 **Keywords:** Astrostatistics (1882); Black hole physics (159); Galaxies (573); Galaxy evolution (594);  
34 Galaxy formation (595); Galaxy physics (612); Galaxy properties (615); Scaling relations  
35 (2031); Supermassive black holes (1663);

## 1. INTRODUCTION

Corresponding author: Zehao Jin (金泽灏)

zj448@nyu.edu

\* These authors contributed equally to this work.

37 Purely observational sciences have long relied on cor-  
38 relations between variables to assess the validity of the-  
39 oretical models. However, observed correlations be-  
40 tween two variables do not provide information about  
41 the direction of causality, making it impossible to dis-  
42 criminate between different causal mechanisms that pre-  
43 dict the same correlational trends. While interventions

(such as randomized controlled trials) are commonly used to identify causal factors in laboratory settings, this is rarely possible in observational fields such as astrophysics. Causal inference overcomes this limitation by exploiting the fact that different causal models produce distinct joint distributions of correlated variables with additional observables, allowing us to discriminate between these models and shed light on the direction of causality. With this, it becomes possible to investigate causal relationships in a purely data-driven manner.

The existence of correlations between the mass of central SMBHs and the properties of their host galaxies has long been observationally established (Magorrian et al. 1998; Ferrarese & Merritt 2000; Gebhardt et al. 2000) and reproduced by specific prescriptions in numerical simulations (Soliman et al. 2023). However, unveiling the causal structure underpinning these correlations has remained an open problem: does galaxy evolution influence the growth of SMBHs by regulating accretion, or do SMBHs shape their host galaxies' properties via feedback (Di Matteo et al. 2005; Kormendy & Ho 2013; Heckman & Best 2014; Silk & Rees 1998; Sijacki et al. 2007; Di Matteo et al. 2008; Schaye et al. 2010; Gaspari et al. 2013)? With the advent of the *James Webb Space Telescope*, this debate has been reinvigorated by the detection of massive high-redshift quasars (Larson et al. 2023).

The few attempts at identifying causal relations in the astrophysical literature focus on two variables at a time or on estimating causal coefficients given a causal structure (causal inference). Pasquato & Matsiuk (2019) used a regression discontinuity approach (Imbens & Lemieux 2008) to measure the causal effect of galactic disk-shocking (Ostriker et al. 1972) on open star cluster properties. A similar approach was followed by Pang et al. (2021) to measure the causal effect of a supernova explosion in the Vela OB2 complex on star formation.

Ellison et al. (2019) used a matching strategy to measure the causal effect of galaxy mergers on active galactic nuclei (AGNs) activity. Matching is a popular way of controlling for confounds in quasi-experimental data, where assignment to treatment is not determined at random (Greenwood 1945). A precursor to matching in the astrophysical literature is the study of “second-parameter pairs” in globular clusters (Catelan et al. 2001): globular clusters were matched based on metallicity and other properties, looking for the reason one member of the pair displayed a hot horizontal branch and its match would not.

Bluck et al. (2022) utilized a Random Forest classifier to extract causal insights from observations to find the most predictive parameters associated with the quench-

ing of star formation. Gebhard et al. (2022) applied a de-noising technique based on causal principles, half-sibling regression (Schölkopf et al. 2016), to exoplanet imaging. In physics, outside of the context of astronomy and cosmology, causal techniques have found direct application in geophysics (Runge et al. 2019) and climate science (Di Capua et al. 2020), and have functioned as a basis for theoretical development in quantum foundations (Spekkens 2023; Allen et al. 2017; Leifer & Spekkens 2013; Wood & Spekkens 2015) and thermodynamics (Janzing 2007; Allahverdyan & Janzing 2008). Our work builds upon a preliminary pilot study to explore causal connections in galaxy–SMBH systems (Pasquato et al. 2023).

In this paper, we present a first-of-its-kind causal study of galaxies' and their SMBHs, ultimately finding a compelling data-driven result. In the main text, we provide an overview of our data sample (§2), a concise description of the causal structures we find (§3), discuss our findings as they pertain to galaxy evolution (§4.1) and AGNs feedback (§4.2), double check our results with alternate tests (§5), and conclude by offering some insights and future directions. (§6). Throughout a comprehensive appendix, we further provide a primer on causal inference/discovery (§A), a detailed accounting of our data (§B), our Bayesian methodology (§C), our statistical analysis (§D), more information on semi-analytical models (§E), constraint-based verifications (§F), consideration of unobserved confounders (§G), inclusion of observational errors (§H), outlier analysis (§I), approximations (§J), and an investigation of cyclicity (§K). All uncertainties are quoted at  $1\sigma \equiv 68.3\%$  confidence intervals.

## 2. DYNAMICALLY-MEASURED SMBH HOST GALAXIES

To explore the causal relationship between SMBHs and their host galaxies, we use the state-of-the-art dataset of a sample of 101 galaxies and their dynamically measured SMBH masses. The dataset comprises seven variables of interest: dynamically-measured black hole mass ( $M_\bullet$ ), central stellar velocity dispersion ( $\sigma_0$ ), effective (half-light) radius of the spheroid<sup>1</sup> ( $R_e$ ), the average projected density within  $R_e$  ( $\langle \Sigma_e \rangle$ ), total stellar mass ( $M^*$ ), color ( $W2 - W3$ ), and specific star formation rate (sSFR). Among these seven variables,  $\sigma_0$ ,  $R_e$ , and  $\langle \Sigma_e \rangle$  cover the fundamental plane of elliptical galaxies (Djorgovski & Davis 1987); while  $M^*$ ,  $W2 - W3$ , and

<sup>1</sup> Throughout this paper, we use the terms “bulge” and “spheroid” interchangeably to refer to the spheroid component of spiral and lenticular galaxies or the entirety of pure elliptical galaxies.

<sup>143</sup> sSFR capture the star formation (see §B).  $M_{\bullet}$  values  
<sup>144</sup> are curated from the literature on dynamical black hole  
<sup>145</sup> mass measurements, and  $\sigma_0$  values are obtained from  
<sup>146</sup> the HyperLeda database (Makarov et al. 2014).  $R_e$  and  
<sup>147</sup>  $\langle \Sigma_e \rangle$  measurements come from multi-component decom-  
<sup>148</sup> positions of surface brightness light profiles (primarily  
<sup>149</sup> of 3.6  $\mu\text{m}$  *Spitzer* Space Telescope imaging) from suc-  
<sup>150</sup> ceeding works (Savorgnan & Graham 2016; Davis et al.  
<sup>151</sup> 2019a; Sahu et al. 2019a; Graham & Sahu 2023a).  $M^*$ ,  
<sup>152</sup>  $W2 - W3$ , and sSFR are from the Wide-field Infrared  
<sup>153</sup> Survey Explorer, WISE (Wright et al. 2010).

<sup>154</sup> The data has been used in a series of work related to  
<sup>155</sup> black hole mass scaling relations (Graham & Scott 2013;  
<sup>156</sup> Scott et al. 2013; Savorgnan et al. 2013, 2016; Sahu et al.  
<sup>157</sup> 2019a,b, 2020; Graham & Sahu 2023b; Davis et al. 2017,  
<sup>158</sup> 2018, 2019a,b; Davis & Jin 2023, 2024), and more de-  
<sup>159</sup>tailed information about the data can be found in §B.  
<sup>160</sup> To investigate the effect of galaxy morphologies on the  
<sup>161</sup> underlying causal structure, we further split our sample  
<sup>162</sup> into 35 elliptical (E), 38 lenticular (S0), and 28 spiral  
<sup>163</sup> (S) galaxies. This choice is motivated by the observed  
<sup>164</sup> difference in intrinsic scatter ( $\epsilon$ ) in the  $M_{\bullet}$ - $\sigma_0$  relation  
<sup>165</sup> (Ferrarese & Merritt 2000; Gebhardt et al. 2000) in el-  
<sup>166</sup> liptical ( $\epsilon = 0.31$  dex) vs. spiral galaxies ( $\epsilon = 0.67$  dex)  
<sup>167</sup> (Sahu et al. 2019b) and this choice is consistent with  
<sup>168</sup> current understanding of quenching and hierarchical as-  
<sup>169</sup>sembly (Springel et al. 2005).

### 170 3. A COMPENDIUM OF CAUSAL STRUCTURES

<sup>171</sup> To represent the causal structure of the dataset, we  
<sup>172</sup> use Directed Acyclic Graphs (DAGs). Each DAG en-  
<sup>173</sup>codes a set of conditional independencies, and DAGs  
<sup>174</sup>that encode the same conditional independencies belong  
<sup>175</sup>to the same Markov Equivalence Class (MEC)<sup>2</sup>. This  
<sup>176</sup>choice assumes that no cyclical dependencies between  
<sup>177</sup>variables exist. This is a reasonable assumption, given  
<sup>178</sup>the clear differences in gas fractions and merger histories  
<sup>179</sup>between the different morphological classes (see §K for  
<sup>180</sup>more details). To achieve a purely data-driven study,  
<sup>181</sup>we adopt a uniform prior, giving equal prior probabili-  
<sup>182</sup>ty,  $P(G)$ , to every one of the nearly  $1.14 \times 10^9$  possi-  
<sup>183</sup>ble DAGs (OEIS Foundation Inc. 2024a). We calculate  
<sup>184</sup>the exact posterior probabilities of every DAG given the  
<sup>185</sup>data,  $P(G | D)$ , using the Bayesian Gaussian equivalent  
<sup>186</sup>(BGe) score (Geiger & Heckerman 1994, 2002; Kuipers  
<sup>187</sup>et al. 2014). The BGe score gives the marginal likeli-  
<sup>188</sup>hood by examining conditional independencies and en-  
<sup>189</sup>sures that DAGs belonging to the same MEC are scored  
<sup>190</sup>equally.

<sup>2</sup> See §A for a brief introduction to causal inference.

<sup>191</sup> Among all possible causal structures, the most prob-  
<sup>192</sup>able MEC and its corresponding DAGs for E, S0, and S  
<sup>193</sup>galaxies are shown in Figure 1. More detailed informa-  
<sup>194</sup>tion about the DAGs, MECs, and their exact posterior  
<sup>195</sup>distributions can be found in §C. We find that in the  
<sup>196</sup>most probable MEC for elliptical galaxies, the SMBH  
<sup>197</sup>mass is a causal child, i.e., an effect of galaxy properties,  
<sup>198</sup>while in the most probable MEC for spirals, the SMBH  
<sup>199</sup>mass is a parent of galaxy properties (with lenticulars  
<sup>200</sup>being in the middle).

<sup>201</sup> The morphologically-dependent set trend holds not  
<sup>202</sup>only in the most probable graphs but is common over  
<sup>203</sup>the entire posterior distribution. This can be quantified  
<sup>204</sup>using edge and path marginals. Edge marginals are the  
<sup>205</sup>posterior probability of a direct causal relation between  
<sup>206</sup>two variables, marginalized over the causal structures of  
<sup>207</sup>the other nodes. Similarly, path marginals provide the  
<sup>208</sup>probability of a causal connection between two variables  
<sup>209</sup>through a potentially indirect path (e.g., through inter-  
<sup>210</sup>mediate nodes). These marginal causal structures can  
<sup>211</sup>be represented in matrix form as shown in Figure 2. The  
<sup>212</sup>first row ( $M_{\bullet} \rightarrow \text{galaxy}$ ) and column ( $\text{galaxy} \rightarrow M_{\bullet}$ ) of  
<sup>213</sup>each matrix contain information pertaining to the in-  
<sup>214</sup>ferred causal relationship between SMBH masses and  
<sup>215</sup>their host galaxy properties.

<sup>216</sup> Among all possible DAGs, the percentage of graphs  
<sup>217</sup>exhibiting a direct edge from  $\sigma_0$  to  $M_{\bullet}$  is 78% in el-  
<sup>218</sup>lipticals, 72% in lenticulars, and only 22% in spirals.  
<sup>219</sup> The path marginals in the bottom row support a simi-  
<sup>220</sup>lar picture, as by considering all possible paths relating  
<sup>221</sup>these two nodes, we find that 79% of DAGs in ellip-  
<sup>222</sup>cals and 72% in lenticulars have  $\sigma_0$  as an ancestor of  
<sup>223</sup> $M_{\bullet}$ , whereas this is the case in only 25% of DAGs in  
<sup>224</sup>spirals. For comparison, the null results (i.e., the poste-  
<sup>225</sup>rior from a uniform prior without any data) for the edge  
<sup>226</sup>marginals are  $P(\text{Parent}) = 29\%$ ,  $P(\text{Child}) = 29\%$ , and  
<sup>227</sup> $P(\text{Disconnected}) = 42\%$ ; for the path marginals these  
<sup>228</sup>probabilities are  $P(\text{Ancestor}) = 42\%$ ,  $P(\text{Descendant}) =$   
<sup>229</sup>42%, and  $P(\text{Disconnected}) = 16\%$  (see §D).

### 230 4. FINDINGS

#### 231 4.1. Causal Connections for Galaxy Evolution

<sup>232</sup> We find that these results are consistent with theoret-  
<sup>233</sup>ical models of galactic evolution. Ellipticals are highly  
<sup>234</sup>evolved galaxies, being the result of a large number of  
<sup>235</sup>galactic mergers. Modern hydrodynamical cosmological  
<sup>236</sup>simulations such as IllustrisTNG (Marinacci et al. 2018;  
<sup>237</sup>Naiman et al. 2018; Nelson et al. 2018; Pillepich et al.  
<sup>238</sup>2018; Springel et al. 2018) show that elliptical galaxies  
<sup>239</sup>with  $\log(M^*/M_{\odot}) \geq 11$  are generally the end result of  
<sup>240</sup>two or more major merger events, such that the typi-  
<sup>241</sup>cal present-day fraction of stars with *ex situ* origins is

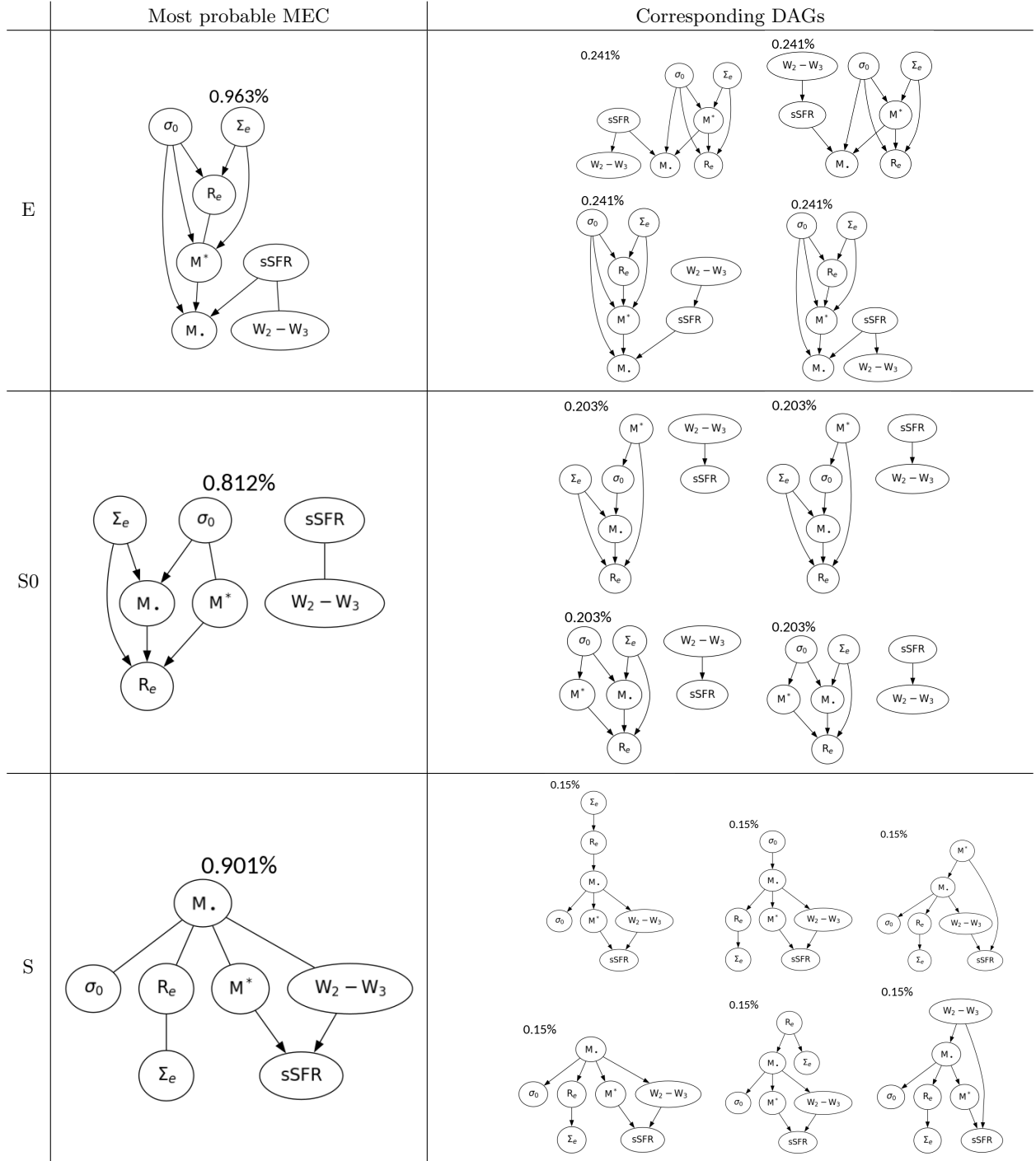


**Figure 1.** The most probable Markov Equivalence Class (MEC) for each morphology and their corresponding Directed Acyclic Graphs (DAGs). MECs are represented as Partially Directed Acyclic Graphs (PDAGs). Directed edges suggest the direction of causality. The undirected edge  $A — B$  suggests both directions are possible (either  $A \rightarrow B$  or  $A \leftarrow B$ ), as long as no new MEC/conditional independencies are introduced by creating new colliders (i.e., two nodes both pointing towards a third node,  $A \rightarrow C \leftarrow B$ ). In the ellipticals,  $M_*$  is strictly a child, while in spiral galaxies,  $M_*$  is *always* connected with four galaxy properties through four undirected edges, suggesting either  $M_*$  is the parent of all of the four galaxy properties, or  $M_*$  is the parent of three of the galaxy properties, and the child of the remaining one (as shown in the corresponding DAGs), ruling out more than one galaxy property pointing towards  $M_*$ , since this creates a new collider and breaks the encoded conditional independencies. The percentage listed above each graph indicates the posterior probability of the graph, whereas the prior probability for each individual DAG is equal to the reciprocal of the total number of DAGs, approximately  $8.78 \times 10^{-10}$  (OEIS Foundation Inc. 2024a). The MEC probabilities are the sum of their corresponding DAGs.

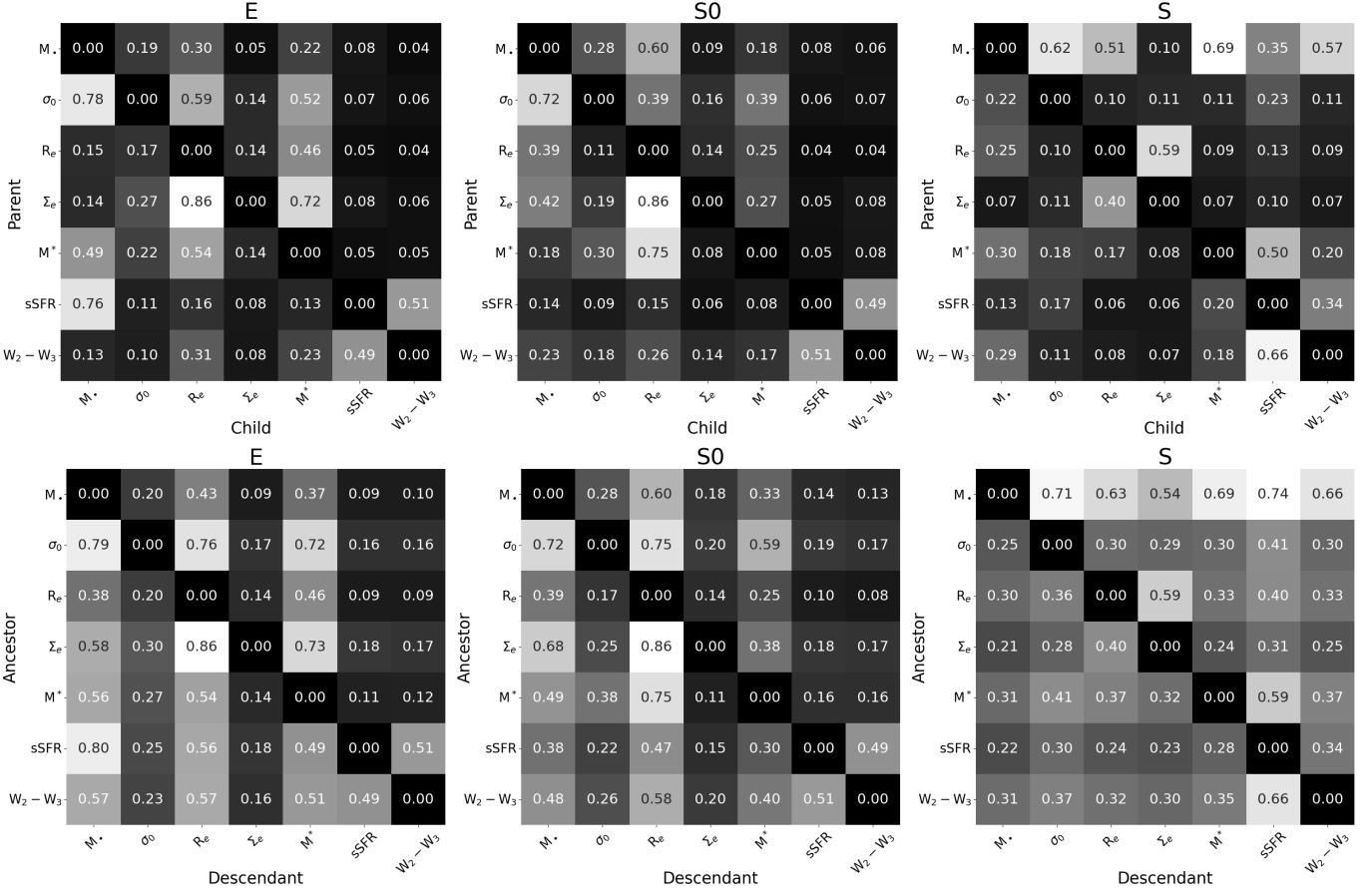


**Figure 2.** Exact posterior edge marginals (top matrices) and path marginals (bottom matrices) for *elliptical* (left matrices), *lenticular* (middle matrices), and *spiral* (right matrices) galaxies. Edge marginals give the probability of Parent → Child through directed edges summed over all DAGs and their probabilities, and path marginals give the probability of Ancestor → Descendant through both direct and indirect paths.

242 greater than 50% (Cannarozzo et al. 2023)<sup>3</sup>. In even  
 243 more general terms, the process of successive mergers  
 244 will act to erase the preexisting causal connection from  
 245 the SMBH to its host galaxy and establish new corre-  
 246 lations via the central limit theorem Jahnke & Macciò  
 247 (2011).

248 During a merger, the SMBHs at the center of each  
 249 merging galaxy play no role in the large-scale dynam-  
 250 ics; it is the galaxy properties (chiefly size and mass)  
 251 that shape the galaxy mergers and their outcomes. Cen-  
 252 tral SMBHs are passively driven to the bottom of the  
 253 post-galaxy-merger potential well by dynamical friction,  
 254 eventually merging together. So it stands to reason  
 255 to expect that in ellipticals, the distribution of SMBH  
 256 masses is determined by that of galaxy properties and  
 257 *not* vice versa.

258 For spiral galaxies, this is not the case, since they ex-  
 259 perience at most a few relatively minor mergers. Unlike  
 260 elliptical galaxies, spirals are predominantly composed  
 261 of *in situ* stellar populations. Causal relations between  
 262 SMBH mass and galaxy properties may thus be set pri-  
 263 mordially in a secular coevolution phase, and they are  
 264 not erased by mergers. As a result, spiral galaxies be-  
 265 have markedly differently compared to ellipticals. In-  
 266 terestingly, lenticulars appear to lie in-between, as ex-  
 267 pected, based on the fact that lenticulars have under-  
 268 gone enough mergers to erase spiral structure while still  
 269 maintaining an extended disk structure, but are not yet  
 270 comparable to ellipticals in terms of mass and pressure  
 271 support.<sup>4</sup> Moreover, by extension of Cannarozzo et al.  
 272 (2023)'s results to all early-type (i.e., lenticular and el-  
 273 liptical) galaxies, all but the most massive lenticular  
 274 galaxies should still maintain *in situ* stellar fractions  
 275 greater than 50%.

276 The six galaxy variables studied here can be split into  
 277 the three parameters defining the fundamental plane  
 278 (FP) of elliptical galaxies and three parameters related  
 279 to star formation. The FP is a manifestation of dy-  
 280 namical equilibrium reached in the largely pressure-  
 281 supported stellar dynamics of massive elliptical galax-  
 282 ies (Mould 2020). Moreover, it is a consequence of the  
 283 merger formation of these galaxies via dissipation and  
 284 feedback that ultimately places them on the FP. Al-  
 285 though only 35/101 of our galaxies are ellipticals, the

286 classical bulges of lenticular and spiral galaxies are also  
 287 governed by the FP. Indeed, it has been found that the  
 288 bulges of type S0–Sbc galaxies tightly follow the same  
 289 FP relation as ellipticals (Falcón-Barroso et al. 2002).

290 The matrices in Figure 2 also provide information  
 291 about the causal nature of the observed FP relationship.  
 292 By looking at the path marginals for elliptical galaxies  
 293 (bottom left), we find that  $\langle \Sigma_e \rangle$  is the ancestor (86%)  
 294 of  $R_e$  and that  $\sigma_0$  is an ancestor (76%) of  $R_e$ . This  
 295 implies  $\langle \Sigma_e \rangle$  and  $\sigma_0$  are both upstream of  $R_e$ , confirm-  
 296 ing that the density and dynamics of stellar populations  
 297 in an elliptical galaxy govern its size. Furthermore, we  
 298 find that there is nearly no chance that  $M^*$  is discon-  
 299 nected from  $R_e$  (i.e., 54% + 46% = 100%, they are *never*  
 300 *d*-separated, thus *always* correlated), indicating the ex-  
 301 istence of a size–mass relation due to the virial theorem  
 302 (i.e.,  $M \sim \sigma^2 R$ ).

#### 303 4.2. Causal Active Galactic Nuclei Feedback

304 From Figure 2, we find that, in spirals,  $M_\bullet$  is the  
 305 ancestor (74%) of sSFR, in lenticulars, there is no domi-  
 306 nant causal direction between the two parameters (38%  
 307 and 14%), while in ellipticals,  $M_\bullet$  becomes the descen-  
 308 dant (80%) of the galaxy's sSFR. This can be interpreted  
 309 as a direct consequence of the presence or absence of  
 310 gas through AGNs feedback. If there is a substantial  
 311 gas reservoir (as in spirals), the SMBH is the ances-  
 312 tor since its feedback is responsible for shutting down  
 313 star formation and hence stopping the growth of stellar  
 314 mass. With a dearth of gas, as in ellipticals, even large  
 315 AGNs bursts will not affect the stellar mass, and thus  
 316 the SMBH cannot be an ancestor of galaxy properties.  
 317 This is further supported by the fact that we find that  
 318  $M_\bullet$  is the parent (69%) of  $M^*$  in spirals, but becomes  
 319 the descendant (56%) or child (49%) of  $M^*$  in elliptical  
 320 galaxies. However, it is true that in the absence of gas,  
 321 mergers are the main pathway for SMBH growth, and  
 322 this will also cause the SMBH to become a descendant or  
 323 child in hierarchical assembly (Jahnke & Macciò 2011;  
 324 Graham & Sahu 2023b; Graham 2023b).

## 325 5. ADDITIONAL TESTS

### 326 5.1. Controlling Feedback with Semi-analytic Models

327 We performed multiple verification tests of our results.  
 328 We tested the same causal discovery approach on a set  
 329 of semi-analytic models (SAMs) of galaxies with cen-  
 330 tral black holes that have a clearly-defined (and cus-  
 331 tomizable) causal direction for galaxy–SMBH coevo-  
 332 lution (see more details in §E). In SAM galaxies, black hole  
 333 feedback is actively affecting galaxies and is hard-coded  
 334 to turn off as soon as a galaxy is quenched. There-  
 335 fore, in SAM elliptical galaxies that become quenched,

<sup>3</sup> Here, Cannarozzo et al. (2023) follow previous work (Rodríguez-Gómez et al. 2015, 2016) and define a major merger as a stellar mass ratio greater than 1/4 between the two progenitors of a given galaxy.

<sup>4</sup> The coevolution of lenticular galaxies and their black holes is also strongly influenced by the presence of dust (Graham 2023a, 2024).

336 galaxy properties cause the black hole mass via the only  
 337 remaining mechanism (i.e., mergers/accretion), and in  
 338 SAM spiral galaxies with black hole feedback still on,  
 339 black holes primarily cause galaxy properties. We con-  
 340 ducted an additional check where the black hole feed-  
 341 back is manually turned off throughout the entire life of  
 342 galaxies as “SAM no feedback” galaxies. The results we  
 343 present in Figure 3 indeed confirm the designed causal  
 344 structure in the SAMs.

### 345 5.2. Crosschecking, Confounders, Errors, & Outliers

346 We also crosscheck our results with two alternative  
 347 causal discovery methods, both *constraint-based*: the  
 348 Peter-Clark, PC, (Spirtes et al. 2000) algorithm and the  
 349 Fast Causal Inference, FCI, (Spirtes 2001) algorithm,  
 350 which both yield consistent results with the exact pos-  
 351 terior approach (see §F). Additionally, we test the inclu-  
 352 sion of the distance to galaxies as a substitute variable,  
 353 exploring the possibility of it being a hidden confounder  
 354 (see §G). We find that the causal relations identified  
 355 are not altered. Furthermore, we find that the inferred  
 356 causal relations are robust to observational errors using  
 357 random sampling (see §H) and to possible outlier galax-  
 358 ies using leave-one-out cross-validation (see §I).

### 359 5.3. Possible Extension to More Variables

360 The exact posterior methodology employed here for  
 361 causal discovery is a powerful tool for ascertaining causal  
 362 structures in a purely data-driven manner. However,  
 363 for problems with more variables, this exact approach  
 364 becomes computationally intractable due to the combi-  
 365 natorial increase in the number of possible DAGs. In  
 366 these cases, it remains possible to quantify the posterior  
 367 over DAGs through posterior samples generated with  
 368 samplers such as DAG-GFN (Deleu et al. 2022), built on  
 369 GFlowNets (Bengio et al. 2021, 2023). We sampled the  
 370 posterior by training a DAG-GFN, giving results consis-  
 371 tent with the exact-posterior approach (see §J).

## 372 6. CONCLUSIONS

373 We present the first data-driven evidence on the di-  
 374 rection of the causal relationship between supermassive  
 375 black holes and their host galaxies. Our findings re-  
 376 veal that in elliptical galaxies, bulge properties influence  
 377 SMBH growth, whereas in spiral galaxies, SMBHs shape  
 378 galaxy characteristics. The process of quenching can be  
 379 causally explained as follows:

- 380 1. quenching starts in gas rich (i.e., spiral) galaxies,  
   and hence there is a causal connection; and
- 382 2. the quenching is over in elliptical galaxies, where  
   we only see the end product of such quenching,  
   and the causal connection is now reversed.

385 These findings support theoretical models of galactic  
 386 evolution driven by feedback processes and mergers.  
 387 Further insights can be gained by using time-series data  
 388 and control variables in galaxy simulations (Waterval  
 389 et al. 2024) to test the causal findings and explanations  
 390 presented here.

391 With knowledge of the underlying causal structures  
 392 and mechanisms behind galaxy–SMBH coevolution, it  
 393 should ultimately be possible to create physically-  
 394 motivated black hole mass scaling relations. The suc-  
 395 cessful application of causal discovery to this astrophys-  
 396 ical dataset paves the way for a deeper understanding of  
 397 the fundamental physical processes driving galaxy evolu-  
 398 tion and establishes causal discovery as a powerful tool  
 399 for data-driven breakthroughs across various scientific  
 400 disciplines.

401 This research was carried out on the high-performance  
 402 computing resources at New York University Abu  
 403 Dhabi. We acknowledge the usage of the HyperLeda  
 404 database (<http://leda.univ-lyon1.fr>). Z.J. and M.P.  
 405 wish to extend their heartfelt thanks to Jithendaraa  
 406 Subramanian for providing in-depth support and clar-  
 407 ifications regarding DAG-GFN, and to Michelle Liu for  
 408 comments and discussion. Y.H. thanks Andrew Benson  
 409 and Dhanya Sridhar for helpful discussions. Z.J. thanks  
 410 Michael Blanton and Joseph Gelfand for useful sugges-  
 411 tions. Z.J. genuinely thanks Mohamad Ali-Dib for his  
 412 very timely help with HPC technical issues.

413 This material is based upon work supported by  
 414 Tamkeen under the NYU Abu Dhabi Research Insti-  
 415 tute grant CASS. This work is partially supported by  
 416 Schmidt Futures, a philanthropic initiative founded by  
 417 Eric and Wendy Schmidt as part of the Virtual In-  
 418 stitute for Astrophysics (VIA). M.P. acknowledges fi-  
 419 nancial support from the European Union’s Horizon  
 420 2020 research and innovation program under the Marie  
 421 Skłodowska-Curie grant agreement No. 896248.

422 The data and code used for this work are available for  
 423 download from the following GitHub repository: <https://github.com/ZehaoJin/causalbh>.

### 425 Software:

426 **causal-learn** (Zheng et al. 2023)

427 **DAG-GFN** (Deleu et al. 2022)

428 **Gym** (Brockman et al. 2016)

429 **JAX** (Bradbury et al. 2018)

430 **Matplotlib** (Hunter 2007)

431 **NetworkX** (Hagberg et al. 2008)

432 **NumPy** (Harris et al. 2020)

433 **Pandas** (McKinney 2010)

434 **pgmpy** (Ankan & Panda 2015)

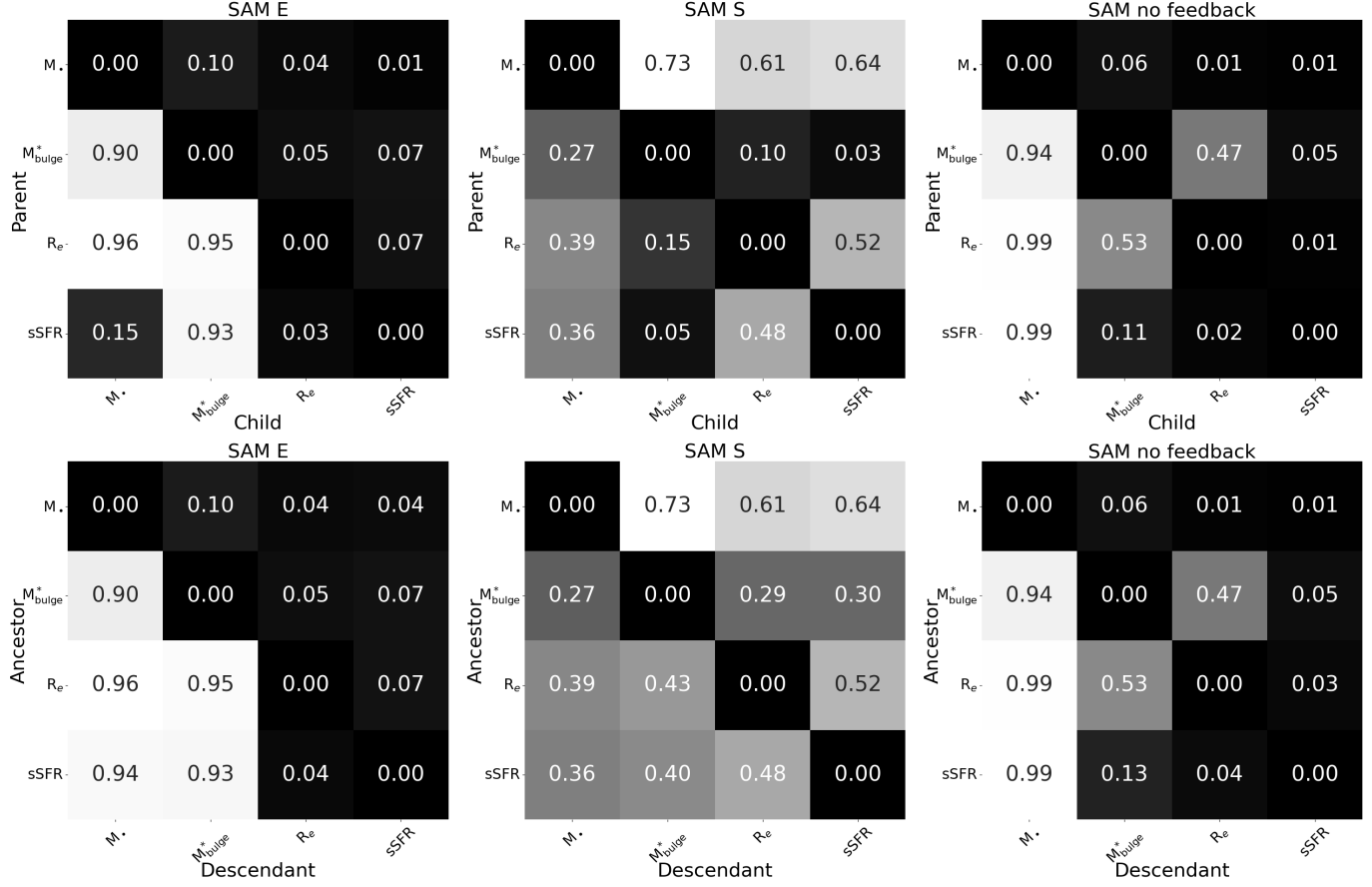


**Figure 3.** Edge (top matrices) and path (bottom matrices) marginals for SAM galaxies. These matrices are similar to those found in Figure 2. Causal discovery is performed on ellipticals (SAM E), spirals (SAM S), and galaxies with black hole feedback intentionally turned off (SAM no feedback). Here, we are restricted to four parameters that are tracked in the SAMs.

<sup>435</sup> PyGraphviz

<sup>437</sup> SciPy (Virtanen et al. 2020)

<sup>436</sup> Python (Van Rossum & Drake 2009)

<sup>438</sup> seaborn (Waskom 2021)

439

## APPENDIX

### A. CAUSAL INFERENCE AND DISCOVERY

<sup>440</sup> The seminal book *Causality* (Pearl 2009) introduced operational definitions for the presence of several types of causal relations between different variables.<sup>5</sup> While these build on empirically observable statistical dependencies between pairs of variables, they leverage the presence of additional variables to break the symmetry inherent in such associations. For instance, if variables  $X$  and  $Y$  are dependent when conditioning on any set of other variables  $S$  (that is, they are persistently associated) and there exists a third variable  $Z$  such that (conditional on some  $S$ )  $X$  and  $Z$  are independent while  $Z$  and  $Y$  are dependent (there is something else, independent of  $X$ , with which  $Y$  is associated), then  $X$  is dubbed a *potential cause* of  $Y$ . In addition to *potential cause*, *Causality* (Pearl 2009) also defines the notions of *genuine cause* and *spurious association*.

<sup>5</sup> We refer the interested reader to Pearl et al. (2016) and two online courses found at <https://www.bradyneal.com/causal-inference-course> and <https://www.bilibili.com/video/BV1sJ41177sg> for further information about causal inference.

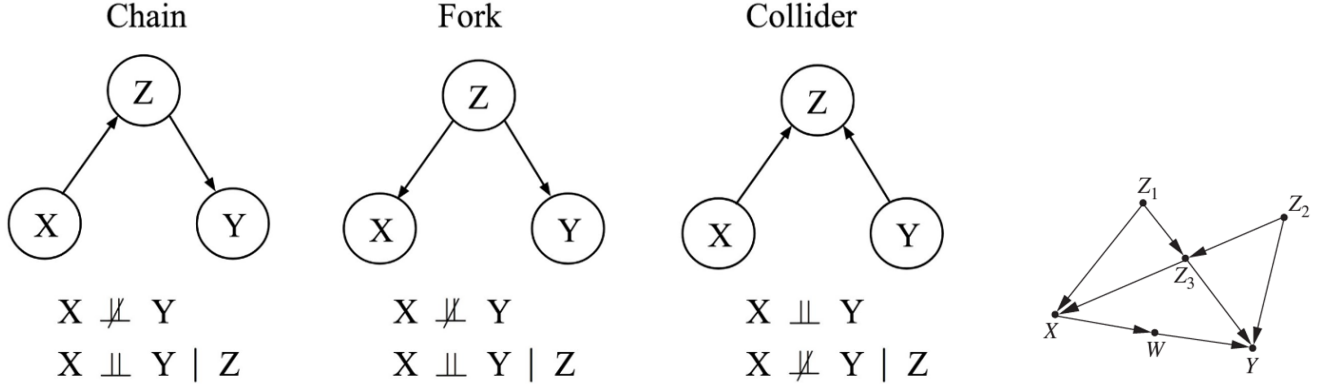


**Figure 4.** Three basic causal models, their (conditional) independencies, and a more complex graph on the right.

449

#### A.1. Basic Causal Structures

450 In the case of causally-related variables, there are three basic causal structures that can be represented as DAGs:  
 451 *chains*, *forks*, and *colliders* (Figure 4).

- 452 • In the case of a *chain*,  $X$  causes ( $\rightarrow$ )  $Z$ , and  $Z$  causes ( $\rightarrow$ )  $Y$ . In a chain model,  $X$  and  $Y$  are *not* independent  
 453 ( $X \not\perp\!\!\!\perp Y$ ) without conditioning on  $Z$ . For example, consider three standing dominoes in order  $X$ ,  $Z$ , and  $Y$ .  
 454 The falling of  $X$  will cause  $Z$  to fall, which in turn will cause  $Y$  to fall. However, when we condition on  $Z$ , the  
 455 other two variables,  $X$  and  $Y$ , will be independent ( $X \perp\!\!\!\perp Y | Z$ ). In other words, if we let domino  $Z$  fall, the  
 456 subsequent domino  $Y$  will fall regardless of whether the prior domino  $X$  fell or not.
- 457 • In the case of a *fork*, a single variable  $Z$ , called a confounder, causally influences two other variables  $X$  and  $Y$ .  
 458 For instance, consider the influence of rainy weather ( $Z$ ) on both umbrella sales ( $X$ ) and the number of people  
 459 jogging outside ( $Y$ ). On rainy days, more umbrellas are likely to be sold, and less people will go out for a jog. In  
 460 a fork model, without conditioning on the confounder  $Z$ , the other variables,  $X$  and  $Y$ , will be dependent on each  
 461 other ( $X \not\perp\!\!\!\perp Y$ ). If one were to analyze umbrella sales and jogging activity without considering the weather, they  
 462 will find them to be dependent. However, once we condition on the confounder  $Z$  and compare days with the  
 463 same weather condition, umbrella sales and jogging activity should be independent of each other ( $X \perp\!\!\!\perp Y | Z$ ).
- 464 • A *collider* refers to the case that two variables,  $X$  and  $Y$ , independently cause a third variable  $Z$ . Consider the  
 465 tossing of two fair coins  $X$  and  $Y$ , and a bell  $Z$  that rings whenever both coins lands on heads (this example is  
 466 still valid when  $Z$  is a bell that rings whenever at least one of the coins lands on heads, see Pearl et al. (2016)  
 467 for a detailed Bayesian proof). Without revealing if the bell rings or not, the head/tail states of two coins are  
 468 independent to each other ( $X \perp\!\!\!\perp Y$ )—simply as how coin tosses naturally works. However, if we condition on  
 469 the bell  $Z$  not ringing, knowing one of the coins landed on heads immediately informs us that the other coin  
 470 landed on tails ( $X \not\perp\!\!\!\perp Y | Z$ ), otherwise the bell would have rung.

471 These three causal models each encode (conditional) independencies as discussed above and summarized in Figure 4.  
 472 Notice that chains and forks share the same (conditional) independencies, while colliders have a different set of  
 473 (conditional) independencies. Chains and forks are then considered as the same Markov Equivalence Class (MEC),  
 474 while colliders belong to a different MEC. Note that these examples operate under the Markov assumption:  $X \perp\!\!\!\perp_{\text{Graph}} Y | Z \Rightarrow X \perp\!\!\!\perp_{\text{Data}} Y | Z$ , meaning that the (conditional) independencies encoded in a causal graph should appear in  
 475 its data.<sup>6</sup>

477

#### A.2. Composite Causal Structures

478 In cases with more than three variables, such as in the right side of Figure 4, variables can potentially be connected  
 479 through multiple paths, with several chains, forks, or colliders. Following the (conditional) independencies encoded

<sup>6</sup> Here, we are referring to the global Markov assumption, which is implied by the local Markov assumption. The local Markov assumption states that given its parents in a DAG, a node  $X$  is independent of all its non-descendants.

480 by chains, forks, and colliders, a path is *blocked* when conditioning on the middle variable of a chain or a fork and  
 481 *unblocked* when not conditioning on the middle variable of a chain or a fork. Furthermore, a path is *blocked* when not  
 482 conditioning on the middle variable of a collider and *unblocked* when conditioning on the middle variable of a collider.  
 483 Two variables are defined to be *d-separated* if every path between them is blocked. Thus, *d-separated* variables are  
 484 independent.<sup>7</sup>

485 In the Figure 4, one will find  $Z_2 \not\perp\!\!\!\perp X$  without any conditioning, since there is an unblocked chain path  $Z_2 \rightarrow Z_3 \rightarrow X$ . One should also find  $Z_2 \perp\!\!\!\perp X | (Z_3, Z_1)$ . Conditioning on  $Z_3$  blocks the  $Z_2 \rightarrow Z_3 \rightarrow X$  chain. Over the  
 486  $Z_2 \rightarrow Z_3 \leftarrow Z_1 \rightarrow X$  path, although conditioning on  $Z_3$  unblocks the  $Z_2 \rightarrow Z_3 \leftarrow Z_2$  collider, the conditioning on  $Z_1$   
 487 blocks the  $Z_3 \leftarrow Z_1 \rightarrow X$  fork, making this path blocked. The remaining  $Z_2 \rightarrow Y \leftarrow W \leftarrow X$  path is blocked by the  
 488 collider  $Z_2 \rightarrow Y \leftarrow W$  without conditioning on  $Y$ . Similarly,  $Z_2 \not\perp\!\!\!\perp X | (Z_3, Z_1, Y)$ .

### 490 A.3. Causal Discovery from Observational Data

491 Causal discovery is most easily achieved through interventions. However, in observational fields such as astrophysics,  
 492 interventions are rarely possible (Cheng et al. 2018). In these cases, the field of causal discovery aims to reveal the  
 493 causal relations between variables from purely observational data without interventions using alternative strategies.

#### 494 A.3.1. Constraint-based Methods

495 One of the most straightforward approaches to discovering causal structures from observational data is conducting  
 496 conditional independence tests among variables since different MECs encode distinct conditional independencies.<sup>8</sup>

497 These approaches are generally referred to as *constraint-based methods*.

498 A commonly used constraint-based method is the Peter-Clark (Spirtes et al. 2000), PC, algorithm. The PC algorithm  
 499 consists of three steps:

- 500 1. Start with a fully-connected, undirected graph among all variables, and remove edges based on conditional  
 501 independence tests to arrive at a graph skeleton.
- 502 2. Identify colliders with conditional independence tests and orient them.
- 503 3. Orient edges that are incident on colliders such that no new colliders will be constructed.

504 Note that in addition to the Markov assumption and faithfulness assumption, the PC algorithm further assumes causal  
 505 sufficiency (i.e., no unobserved confounders) and acyclicity.

506 Another constraint-based method, the Fast Causal Inference (Spirtes 2001), FCI, algorithm relaxes the assumption  
 507 of causal sufficiency, allowing unobserved confounders. The FCI algorithm is based on the same independence testing  
 508 procedure as the PC algorithm but differs at the stage of labeling and orienting edges.

509 It has also been proven that PC and FCI algorithms are sound and complete under cyclic settings (M. Mooij &  
 510 Claassen 2020). However, these methods only provide a point estimate for the true MEC without quantifying their  
 511 uncertainties; this becomes particularly problematic when the number of data points is small and the reliability of  
 512 conditional independence tests degrades.

#### 513 A.3.2. Score-based Methods

514 Instead of finding a single causal structure, we can adopt a Bayesian perspective and define a posterior over all possible  
 515 DAGs,  $P(G | D)$ . To do this, *score-based methods* assign a numerical score to every DAG given the data. There are  
 516 several possible ways to define such a score, such as the Bayesian Information Criterion (BIC) score (Chickering 2002),  
 517 generalized score (Huang et al. 2018), and the Bayesian Gaussian equivalent (BGe) score (Geiger & Heckerman 1994,  
 518 2002; Kuipers et al. 2014).<sup>9</sup>

519 In an exact posterior approach, one evaluates the chosen score for every possible DAG, i.e.,  $P(G | D)$ . However,  
 520 the cost of an exact search grows super-exponentially as the number of variables (nodes) increases. For example, the  
 521 number of possible DAGs for three variables is only 25 but exceeds  $4 \times 10^{18}$  for ten variables<sup>10</sup>, making an exact

<sup>7</sup> With the exception of intransitive cases (Pearl et al. 2016).

<sup>8</sup> Here, we adopt the faithfulness assumption, or the converse of  
 the Markov assumption:  $X \perp\!\!\!\perp_{\text{Data}} Y | Z \Rightarrow X \perp\!\!\!\perp_{\text{Graph}} Y | Z$ .

<sup>9</sup> The scores listed above are for continuous data. The Bayesian  
 Dirichlet equivalent (BDe) score (Heckerman et al. 1995) is one  
 of the scores for discrete or categorical data.

<sup>10</sup> See the online encyclopedia of integer sequences (OEIS Foundation Inc. 2024a) for the number of DAGs corresponding to  $n$   
 nodes.

522 posterior search quickly computationally intractable. For the current study, the total number of DAGs for seven  
 523 variables is 1,138,779,265, which is at the limit of computational feasibility.

524 As a result, sampling algorithms have been developed to approximate the exact posterior distribution without going  
 525 over all DAGs. Such approximation is often done with Markov Chain Monte Carlo (MCMC) methods, such as the  
 526 MC3 algorithm (Madigan et al. 1995) and **Gadget** (Viinikka et al. 2020). More recently, Deleu et al. (2022) developed  
 527 DAG–GFn as an alternative to MCMC, and showed that DAG–GFn compares favorably against other methods based on  
 528 MCMC. Here, we also show that DAG–GFn does recover the exact posterior distribution fairly well under the SMBH–  
 529 galaxy context in §J. Some benchmark studies on causal discovery algorithms can be found in several references  
 530 (Emezue et al. 2023; Vowels et al. 2022; Menegozzo et al. 2022; Runge et al. 2019; Ahmed et al. 2020; Kalainathan  
 531 et al. 2020; Scutari 2014).

## 532 B. DATA

533 Our data is composed of a current state-of-the-art sample of galaxies with dynamically-measured SMBH masses.  
 534 These include 145 nearby galaxies with a median luminosity distance of 21.5 Mpc that host SMBHs with directly  
 535 resolved spheres of influence. From this parent sample, 101 out of 145 galaxies have all of the seven desired variables  
 536 of interest for our study. We include the three parameters that define the fundamental plane of elliptical galaxies  
 537 (Djorgovski & Davis 1987), i.e., central stellar velocity dispersion ( $\sigma_0$ ), effective (half-light) radius of the spheroid<sup>11</sup>  
 538 ( $R_e$ ), and the average projected density within  $R_e$  ( $\langle \Sigma_e \rangle$ ).  $M_\bullet$  values are compiled by a series of progressive studies  
 539 on black hole mass scaling relations (Graham & Scott 2013; Scott et al. 2013; Savorgnan et al. 2013, 2016; Sahu et al.  
 540 2019a,b, 2020; Graham & Sahu 2023b; Davis et al. 2017, 2018, 2019a,b; Davis & Jin 2023, 2024).  $\sigma_0$  values are collected  
 541 from several works (Davis et al. 2017, 2019b; Sahu et al. 2019b), which are obtained primarily from the HyperLeda  
 542 database (Makarov et al. 2014) and homogenized to produce an estimate of the mean velocity dispersion within an  
 543 aperture of 595 pc.  $R_e$  and  $\langle \Sigma_e \rangle$  measurements were produced via the multi-component decompositions of surface  
 544 brightness light profiles (primarily of 3.6  $\mu\text{m}$  *Spitzer* Space Telescope imaging) from succeeding works (Savorgnan &  
 545 Graham 2016; Davis et al. 2019a; Sahu et al. 2019a; Graham & Sahu 2023a).<sup>12</sup>

546 This choice of parameters also allows us to explore the well-known  $M_\bullet$ – $\sigma_0$  relation (Ferrarese & Merritt 2000;  
 547 Gebhardt et al. 2000). Indeed, one impetus for this study of SMBH–galaxy causality was the significant difference in  
 548 intrinsic scatter ( $\epsilon$ ) observed in elliptical galaxies ( $\epsilon = 0.31$  dex) vs. spiral galaxies ( $\epsilon = 0.67$  dex) as determined by  
 549 Sahu et al. (2019b). This implies that the  $M_\bullet$ – $\sigma_0$  relation is  $\approx 2.3$  times less accurate for predicting SMBH masses in  
 550 spiral galaxies as opposed to elliptical galaxies. As shown in this work, this difference in the scatter of the relationship  
 551 between morphological types foreshadows their inherent dichotomy in causal structures.

552 The remaining parameters we explore concern properties related to the star-formation rate (SFR) in galaxies. For  
 553 this, we consider data from the Wide-field Infrared Survey Explorer (Wright et al. 2010), WISE, to provide the color,  
 554 total stellar masses ( $M^*$ ), and SFRs for our galaxies. These WISE values are all compiled from Graham et al. (2024):  
 555  $M^*$  is derived from the prescriptions of Jarrett et al. (2023) for W1 (3.4  $\mu\text{m}$ ) photometry and colors from WISE;  
 556 and SFRs accounting for activity over the past 100 Myr is assessed via the WISE total integrated fluxes as per the  
 557 calibrations of Cluver et al. (2017). For WISE colors, we considered both W1–W2 (3.4  $\mu\text{m}$  – 4.6  $\mu\text{m}$ ) and W2–W3  
 558 (4.6  $\mu\text{m}$  – 12.1  $\mu\text{m}$ ) colors, but ultimately elected to conduct our analyses with only the latter color, which exhibits a  
 559 greater range of diversity across morphological classes of galaxies. Rather than absolute SFR, we convert to specific  
 560 star-formation rate (sSFR) by normalizing each SFR by the stellar mass of each galaxy (i.e.,  $\text{sSFR} \equiv \text{SFR}/M^*$ ).

561 We split the sample of galaxies into three morphological classes:

- 562 • highly-evolved, massive, gas-poor elliptical (E) galaxies, which have been exposed to the full range of feedback  
 563 and merging processes throughout their long histories spanning large fractions of the age of the Universe,
- 564 • spiral (S) galaxies, at the opposite end of galaxy morphological classification schemes (Jeans 1928; Hubble 1936;  
 565 Graham 2019), which are unlikely to have encountered any major mergers and still retain a large fraction of their  
 566 gas, and

<sup>11</sup> Here, we use the terms “bulge” and “spheroid” interchangeably to refer to the spheroid component of spiral and lenticular galaxies or the entirety of pure elliptical galaxies.

<sup>12</sup>  $R_e$  (and  $\langle \Sigma_e \rangle$ ) is calculated from the equivalent (i.e., geometric-mean) axis surface brightness profile of each galaxy. Radii computed along the equivalent axis of quasi-elliptical isophotes are equal to  $\sqrt{ab}$ , where  $a$  is the semi-major axis and  $b$  is the semi-minor axis of an isophote, and thus produce a circle with the *equivalent* area as the quasi-elliptical isophote.

- lenticular (S0) galaxies, which represent a bridging population between E and S types.

Altogether, this gives us a sample of 35 elliptical, 38 lenticular, and 28 spiral galaxies for a total of 101 galaxies, each with six physical measurements of the host galaxy plus a dynamically-measured SMBH mass (see Table 1 and its pairplot in Figure 5). All morphologies have been determined by the multi-component decompositions of surface brightness light profiles (Savorgnan & Graham 2016; Davis et al. 2019a; Sahu et al. 2019a; Graham & Sahu 2023a). Our general classification scheme defines elliptical galaxies as spheroids (with or without embedded disk components), lenticular galaxies as spheroids with extended disk components (without spiral structure), and spiral galaxies as disk galaxies (with classical bulges, pseudobulges, or no bulges) with spiral structure. For our purposes in this study, we have not considered barred morphologies as a distinct classification element.

**Table 1.** Sample of 101 Galaxies with Dynamical SMBH Mass Measurements

Galaxy	$\log(M_\bullet)$	$\log(\sigma_0)$	$\log(R_e)$	$\log(\langle \Sigma_e \rangle)$	W2–W3	$\log(M^*)$	$\log(\text{sSFR})$
	[M <sub>⊙</sub> ]	[km s <sup>-1</sup> ]	[kpc]	[M <sub>⊙</sub> pc <sup>-2</sup> ]	[mag]	[M <sub>⊙</sub> ]	[yr <sup>-1</sup> ]
(1)	(2)	(3)	(4)	(5)	(6)	(7)	(8)
35 Elliptical Galaxies							
IC 1459	9.38 ± 0.18	2.47 ± 0.01	0.89 ± 0.09	2.89 ± 0.13	0.39 ± 0.06	11.24 ± 0.08	-12.00 ± 0.10
IC 4296	9.10 ± 0.09	2.52 ± 0.01	0.96 ± 0.31	2.87 ± 0.09	0.02 ± 0.08	11.47 ± 0.08	-12.47 ± 0.11
NGC 821	7.59 ± 0.19	2.30 ± 0.01	0.54 ± 0.01	2.91 ± 0.09	0.27 ± 0.13	10.64 ± 0.08	-11.65 ± 0.11
NGC 1275	8.90 ± 0.24	2.39 ± 0.02	1.24 ± 0.31	2.51 ± 0.13	3.00 ± 0.04	11.52 ± 0.09	-9.81 ± 0.11
NGC 1399	8.67 ± 0.06	2.52 ± 0.01	0.76 ± 0.09	3.01 ± 0.09	0.17 ± 0.07	11.23 ± 0.08	-12.72 ± 0.13
NGC 1407	9.65 ± 0.06	2.42 ± 0.01	0.80 ± 0.31	3.03 ± 0.12	0.07 ± 0.09	11.39 ± 0.08	-15.69 ± 0.44
NGC 1600	10.28 ± 0.04	2.52 ± 0.01	1.22 ± 0.09	2.66 ± 0.07	-0.34 ± 0.10	11.71 ± 0.09	-15.23 ± 0.44
NGC 3091	9.61 ± 0.02	2.49 ± 0.01	1.15 ± 0.09	2.61 ± 0.17	-0.21 ± 0.11	11.39 ± 0.09	-15.09 ± 0.44
NGC 3377	8.24 ± 0.23	2.13 ± 0.01	0.36 ± 0.01	2.77 ± 0.07	-0.09 ± 0.08	10.13 ± 0.08	-14.43 ± 0.44
NGC 3379	8.63 ± 0.11	2.31 ± 0.00	0.43 ± 0.31	3.19 ± 0.14	0.12 ± 0.05	10.64 ± 0.08	-14.94 ± 0.44
NGC 3414	8.38 ± 0.05	2.38 ± 0.01	0.47 ± 0.09	3.07 ± 0.15	0.50 ± 0.07	10.63 ± 0.08	-12.05 ± 0.10
NGC 3585	8.49 ± 0.14	2.33 ± 0.01	0.90 ± 0.31	2.67 ± 0.10	0.06 ± 0.09	11.03 ± 0.09	-13.16 ± 0.28
NGC 3607	8.17 ± 0.17	2.35 ± 0.01	0.90 ± 0.31	2.74 ± 0.13	0.73 ± 0.06	11.13 ± 0.08	-11.73 ± 0.09
NGC 3608	8.63 ± 0.10	2.29 ± 0.01	0.66 ± 0.31	2.75 ± 0.09	-0.13 ± 0.10	10.56 ± 0.09	-14.86 ± 0.44
NGC 3842	9.94 ± 0.12	2.49 ± 0.01	1.48 ± 0.09	2.03 ± 0.08	-0.43 ± 0.07	11.45 ± 0.09	-14.80 ± 0.44
NGC 3923	9.47 ± 0.13	2.39 ± 0.01	0.92 ± 0.09	2.80 ± 0.13	-0.03 ± 0.08	11.30 ± 0.08	-15.60 ± 0.44
NGC 4261	9.21 ± 0.08	2.47 ± 0.01	0.84 ± 0.31	2.89 ± 0.10	0.22 ± 0.08	11.17 ± 0.08	-11.99 ± 0.10
NGC 4291	8.97 ± 0.14	2.47 ± 0.01	0.27 ± 0.31	3.35 ± 0.14	0.00 ± 0.09	10.47 ± 0.08	-14.77 ± 0.44
NGC 4374	8.95 ± 0.04	2.44 ± 0.00	1.04 ± 0.31	2.59 ± 0.08	-0.04 ± 0.07	11.14 ± 0.08	-15.44 ± 0.44
NGC 4472	9.36 ± 0.03	2.45 ± 0.00	1.01 ± 0.09	2.81 ± 0.08	0.28 ± 0.12	11.41 ± 0.08	-12.08 ± 0.10
NGC 4473	7.95 ± 0.22	2.25 ± 0.01	0.43 ± 0.31	2.96 ± 0.08	0.15 ± 0.08	10.53 ± 0.08	-12.05 ± 0.11
NGC 4486	9.85 ± 0.02	2.51 ± 0.01	0.85 ± 0.31	3.05 ± 0.08	0.33 ± 0.05	11.31 ± 0.08	-12.02 ± 0.10
NGC 4552	8.67 ± 0.04	2.40 ± 0.01	0.71 ± 0.31	2.68 ± 0.09	0.50 ± 0.10	10.77 ± 0.09	-12.12 ± 0.11
NGC 4621	8.59 ± 0.04	2.36 ± 0.01	0.88 ± 0.09	2.58 ± 0.10	0.42 ± 0.13	10.89 ± 0.08	-11.82 ± 0.10
NGC 4649	9.67 ± 0.10	2.52 ± 0.01	0.80 ± 0.09	3.04 ± 0.09	0.42 ± 0.10	11.24 ± 0.08	-12.02 ± 0.09
NGC 4697	8.10 ± 0.02	2.22 ± 0.00	1.09 ± 0.40	2.03 ± 0.08	0.09 ± 0.06	10.65 ± 0.08	-12.11 ± 0.11
NGC 4889	10.29 ± 0.33	2.59 ± 0.01	1.43 ± 0.09	2.38 ± 0.09	-0.17 ± 0.09	11.72 ± 0.09	-15.02 ± 0.44

**Table 1** *continued*

**Table 1** (*continued*)

Galaxy	$\log(M_\bullet)$	$\log(\sigma_0)$	$\log(R_e)$	$\log(\langle \Sigma_e \rangle)$	W2–W3	$\log(M^*)$	$\log(\text{sSFR})$
	[M $_\odot$ ]	[km s $^{-1}$ ]	[kpc]	[M $_\odot$ pc $^{-2}$ ]	[mag]	[M $_\odot$ ]	[yr $^{-1}$ ]
(1)	(2)	(3)	(4)	(5)	(6)	(7)	(8)
NGC 5077	8.85 ± 0.23	2.40 ± 0.01	0.64 ± 0.09	3.16 ± 0.17	0.22 ± 0.07	11.02 ± 0.08	-11.94 ± 0.10
NGC 5419	9.86 ± 0.14	2.54 ± 0.01	1.01 ± 0.01	2.87 ± 0.09	0.04 ± 0.12	11.64 ± 0.08	-12.47 ± 0.12
NGC 5576	8.20 ± 0.10	2.26 ± 0.01	0.76 ± 0.09	2.52 ± 0.09	-0.23 ± 0.05	10.70 ± 0.08	-15.00 ± 0.44
NGC 5846	9.04 ± 0.04	2.38 ± 0.01	0.98 ± 0.31	2.64 ± 0.10	-0.13 ± 0.08	11.18 ± 0.09	-15.48 ± 0.44
NGC 6251	8.77 ± 0.14	2.49 ± 0.03	1.16 ± 0.09	2.66 ± 0.09	1.05 ± 0.04	11.51 ± 0.08	-11.49 ± 0.09
NGC 7052	9.35 ± 0.02	2.45 ± 0.02	0.77 ± 0.09	3.04 ± 0.07	0.58 ± 0.05	11.22 ± 0.08	-11.69 ± 0.10
NGC 7619	9.35 ± 0.10	2.50 ± 0.01	1.11 ± 0.31	2.52 ± 0.07	-0.01 ± 0.12	11.29 ± 0.08	-15.11 ± 0.44
NGC 7768	9.10 ± 0.15	2.46 ± 0.02	1.32 ± 0.31	2.36 ± 0.09	-0.38 ± 0.05	11.44 ± 0.09	-14.63 ± 0.44
38 Lenticular Galaxies							
NGC 404	5.74 ± 0.10	1.54 ± 0.04	-1.24 ± 0.31	3.64 ± 0.12	1.28 ± 0.05	8.85 ± 0.09	-10.36 ± 0.16
NGC 524	8.68 ± 0.10	2.37 ± 0.01	0.04 ± 0.31	3.83 ± 0.07	0.52 ± 0.06	11.10 ± 0.08	-12.16 ± 0.10
NGC 1023	7.62 ± 0.04	2.29 ± 0.01	-0.41 ± 0.09	4.21 ± 0.09	0.18 ± 0.07	10.61 ± 0.08	-12.35 ± 0.11
NGC 1194	7.82 ± 0.04	2.17 ± 0.07	-0.04 ± 0.40	3.96 ± 0.09	2.83 ± 0.04	10.46 ± 0.08	-9.87 ± 0.09
NGC 1316	8.16 ± 0.22	2.35 ± 0.01	0.14 ± 0.31	3.94 ± 0.30	0.65 ± 0.05	11.43 ± 0.08	-11.96 ± 0.09
NGC 1332	9.16 ± 0.06	2.47 ± 0.02	0.28 ± 0.40	3.68 ± 0.10	0.42 ± 0.05	10.88 ± 0.08	-11.70 ± 0.11
NGC 1374	8.76 ± 0.04	2.25 ± 0.01	0.03 ± 0.31	3.35 ± 0.08	0.12 ± 0.07	10.33 ± 0.08	-14.63 ± 0.44
NGC 2549	7.14 ± 0.23	2.15 ± 0.01	-0.73 ± 0.09	4.25 ± 0.13	0.33 ± 0.06	9.97 ± 0.08	-11.97 ± 0.15
NGC 2778	7.14 ± 0.43	2.19 ± 0.01	-0.63 ± 0.31	3.85 ± 0.14	0.12 ± 0.05	9.89 ± 0.08	-11.70 ± 0.17
NGC 2787	7.60 ± 0.05	2.28 ± 0.01	-0.86 ± 0.31	4.16 ± 0.16	0.59 ± 0.04	9.80 ± 0.08	-11.89 ± 0.14
NGC 3115	8.94 ± 0.31	2.42 ± 0.01	0.19 ± 0.09	3.58 ± 0.08	0.14 ± 0.12	10.63 ± 0.08	-12.60 ± 0.13
NGC 3245	8.30 ± 0.11	2.32 ± 0.02	-0.63 ± 0.09	4.50 ± 0.10	1.09 ± 0.04	10.45 ± 0.08	-11.22 ± 0.09
NGC 3384	7.02 ± 0.20	2.16 ± 0.01	-0.52 ± 0.09	4.29 ± 0.08	0.24 ± 0.05	10.37 ± 0.08	-11.85 ± 0.11
NGC 3489	6.76 ± 0.06	2.02 ± 0.01	-1.02 ± 0.31	4.74 ± 0.09	1.16 ± 0.04	10.14 ± 0.08	-11.24 ± 0.09
NGC 3665	8.76 ± 0.10	2.33 ± 0.02	0.33 ± 0.31	3.57 ± 0.09	1.33 ± 0.04	11.13 ± 0.08	-11.27 ± 0.09
NGC 3998	8.42 ± 0.18	2.42 ± 0.02	-0.51 ± 0.40	4.20 ± 0.10	1.39 ± 0.05	10.30 ± 0.08	-11.18 ± 0.09
NGC 4026	8.26 ± 0.11	2.24 ± 0.01	-0.83 ± 0.40	4.97 ± 0.13	0.52 ± 0.05	10.18 ± 0.08	-13.23 ± 0.39
NGC 4339	7.63 ± 0.12	2.05 ± 0.01	-0.31 ± 0.31	3.48 ± 0.10	0.67 ± 0.14	10.02 ± 0.08	-11.16 ± 0.12
NGC 4342	8.65 ± 0.18	2.38 ± 0.01	-0.29 ± 0.31	3.68 ± 0.07	0.31 ± 0.04	10.10 ± 0.08	-14.40 ± 0.44
NGC 4350	8.87 ± 0.14	2.26 ± 0.01	0.20 ± 0.31	3.08 ± 0.07	0.51 ± 0.06	10.35 ± 0.08	-12.05 ± 0.10
NGC 4371	6.83 ± 0.07	2.11 ± 0.01	-0.15 ± 0.31	3.37 ± 0.19	0.64 ± 0.09	10.38 ± 0.08	-12.02 ± 0.11
NGC 4429	8.18 ± 0.03	2.24 ± 0.01	-0.05 ± 0.31	3.76 ± 0.08	0.86 ± 0.05	10.75 ± 0.08	-11.59 ± 0.09
NGC 4434	7.84 ± 0.05	2.07 ± 0.01	-0.25 ± 0.31	3.59 ± 0.07	0.00 ± 0.06	10.03 ± 0.08	-14.33 ± 0.44
NGC 4459	7.83 ± 0.08	2.24 ± 0.01	-0.01 ± 0.31	3.69 ± 0.11	1.17 ± 0.10	10.56 ± 0.08	-11.12 ± 0.09
NGC 4526	8.66 ± 0.01	2.35 ± 0.02	0.06 ± 0.31	3.73 ± 0.10	1.14 ± 0.05	10.84 ± 0.08	-11.38 ± 0.09
NGC 4564	7.90 ± 0.12	2.19 ± 0.01	-0.38 ± 0.09	3.96 ± 0.09	0.31 ± 0.05	10.12 ± 0.08	-12.54 ± 0.13
NGC 4578	7.28 ± 0.08	2.05 ± 0.02	-0.31 ± 0.31	3.58 ± 0.07	-0.24 ± 0.10	10.05 ± 0.08	-14.35 ± 0.44
NGC 4596	7.90 ± 0.20	2.15 ± 0.01	-0.13 ± 0.09	3.64 ± 0.07	0.34 ± 0.08	10.54 ± 0.08	-11.84 ± 0.09
NGC 4742	7.13 ± 0.15	2.01 ± 0.01	-0.61 ± 0.31	4.28 ± 0.09	0.40 ± 0.05	9.99 ± 0.09	-11.79 ± 0.15
NGC 4762	7.24 ± 0.05	2.15 ± 0.01	-0.74 ± 0.31	4.38 ± 0.07	0.18 ± 0.07	10.56 ± 0.08	-14.86 ± 0.44

**Table 1** *continued*

**Table 1** (*continued*)

Galaxy	$\log(M_\bullet)$	$\log(\sigma_0)$	$\log(R_e)$	$\log(\langle\Sigma_e\rangle)$	W2–W3	$\log(M^*)$	$\log(\text{sSFR})$
	[M $_\odot$ ]	[km s $^{-1}$ ]	[kpc]	[M $_\odot$ pc $^{-2}$ ]	[mag]	[M $_\odot$ ]	[yr $^{-1}$ ]
(1)	(2)	(3)	(4)	(5)	(6)	(7)	(8)
NGC 5018	8.00 ± 0.08	2.33 ± 0.01	0.05 ± 0.31	4.00 ± 0.09	0.89 ± 0.07	11.10 ± 0.08	-11.40 ± 0.09
NGC 5128	7.65 ± 0.13	2.01 ± 0.03	0.04 ± 0.40	3.75 ± 0.07	2.53 ± 0.03	10.86 ± 0.08	-10.61 ± 0.09
NGC 5252	9.03 ± 0.35	2.27 ± 0.06	-0.15 ± 0.31	4.37 ± 0.09	2.27 ± 0.04	11.05 ± 0.08	-10.30 ± 0.09
NGC 5813	8.83 ± 0.04	2.37 ± 0.01	0.32 ± 0.31	3.44 ± 0.10	0.03 ± 0.12	11.10 ± 0.08	-12.49 ± 0.12
NGC 5845	8.41 ± 0.16	2.36 ± 0.01	-0.20 ± 0.31	3.70 ± 0.11	0.53 ± 0.04	10.14 ± 0.08	-11.75 ± 0.11
NGC 6861	9.30 ± 0.22	2.59 ± 0.02	0.41 ± 0.31	3.29 ± 0.14	0.76 ± 0.05	10.84 ± 0.08	-11.81 ± 0.09
NGC 7332	7.06 ± 0.20	2.11 ± 0.01	-0.59 ± 0.40	4.49 ± 0.10	0.46 ± 0.05	10.48 ± 0.08	-11.78 ± 0.11
NGC 7457	6.96 ± 0.26	1.83 ± 0.02	-0.40 ± 0.31	3.32 ± 0.10	0.27 ± 0.11	9.92 ± 0.08	-11.74 ± 0.14
28 Spiral Galaxies							
Circinus	6.22 ± 0.08	2.17 ± 0.05	-0.34 ± 0.03	3.86 ± 0.17	4.02 ± 0.03	10.04 ± 0.09	-9.37 ± 0.13
IC 2560	6.51 ± 0.09	2.14 ± 0.01	-0.21 ± 0.03	3.29 ± 0.15	3.38 ± 0.04	10.43 ± 0.08	-10.01 ± 0.09
NGC 224	8.15 ± 0.19	2.19 ± 0.01	-0.16 ± 0.00	3.67 ± 0.08	2.08 ± 0.04	10.71 ± 0.08	-10.94 ± 0.09
NGC 253	7.00 ± 0.30	1.98 ± 0.08	-0.33 ± 0.01	3.61 ± 0.07	3.81 ± 0.04	10.43 ± 0.08	-9.85 ± 0.09
NGC 1097	8.38 ± 0.09	2.29 ± 0.01	0.13 ± 0.07	3.75 ± 0.07	3.41 ± 0.04	11.22 ± 0.08	-10.04 ± 0.10
NGC 1300	7.86 ± 0.31	2.34 ± 0.06	-0.13 ± 0.10	3.19 ± 0.09	2.91 ± 0.04	10.56 ± 0.08	-10.41 ± 0.09
NGC 1320	6.77 ± 0.16	2.04 ± 0.04	-0.70 ± 0.07	4.24 ± 0.09	3.34 ± 0.04	10.13 ± 0.09	-9.68 ± 0.10
NGC 1398	8.03 ± 0.08	2.29 ± 0.04	0.09 ± 0.04	3.58 ± 0.17	2.14 ± 0.04	11.17 ± 0.08	-10.88 ± 0.09
NGC 2273	6.95 ± 0.06	2.15 ± 0.03	-0.55 ± 0.03	3.77 ± 0.15	3.14 ± 0.04	10.43 ± 0.08	-10.02 ± 0.09
NGC 2960	7.07 ± 0.04	2.22 ± 0.04	-0.13 ± 0.05	3.89 ± 0.09	2.98 ± 0.04	10.72 ± 0.08	-10.42 ± 0.09
NGC 2974	8.23 ± 0.05	2.37 ± 0.01	-0.17 ± 0.01	3.76 ± 0.12	1.36 ± 0.08	10.61 ± 0.08	-11.28 ± 0.09
NGC 3031	7.83 ± 0.09	2.18 ± 0.01	-0.14 ± 0.01	3.65 ± 0.08	1.80 ± 0.03	10.57 ± 0.08	-11.00 ± 0.09
NGC 3079	6.28 ± 0.30	2.24 ± 0.03	-0.46 ± 0.05	4.04 ± 0.17	3.64 ± 0.04	10.41 ± 0.08	-9.84 ± 0.09
NGC 3227	7.25 ± 0.25	2.10 ± 0.02	0.01 ± 0.03	3.38 ± 0.13	3.09 ± 0.04	10.65 ± 0.08	-10.11 ± 0.09
NGC 3368	6.89 ± 0.09	2.07 ± 0.01	-0.60 ± 0.02	4.22 ± 0.14	2.13 ± 0.04	10.55 ± 0.08	-10.81 ± 0.09
NGC 3627	6.94 ± 0.05	2.10 ± 0.02	-0.71 ± 0.07	4.33 ± 0.17	3.44 ± 0.04	10.63 ± 0.08	-10.06 ± 0.09
NGC 4151	7.29 ± 0.37	1.96 ± 0.05	-0.25 ± 0.02	3.97 ± 0.13	2.82 ± 0.04	10.53 ± 0.08	-9.89 ± 0.09
NGC 4258	7.61 ± 0.01	2.12 ± 0.02	-0.01 ± 0.06	3.27 ± 0.07	2.44 ± 0.04	10.56 ± 0.08	-10.59 ± 0.09
NGC 4303	6.78 ± 0.04	1.98 ± 0.04	-0.70 ± 0.02	4.65 ± 0.07	3.87 ± 0.04	10.71 ± 0.09	-9.86 ± 0.10
NGC 4388	6.95 ± 0.09	2.00 ± 0.04	0.09 ± 0.02	3.07 ± 0.19	3.15 ± 0.04	10.12 ± 0.08	-9.85 ± 0.09
NGC 4501	7.31 ± 0.08	2.22 ± 0.02	0.22 ± 0.04	3.22 ± 0.07	3.05 ± 0.04	10.89 ± 0.08	-10.35 ± 0.09
NGC 4594	8.81 ± 0.03	2.35 ± 0.01	0.28 ± 0.02	3.48 ± 0.08	0.90 ± 0.05	11.06 ± 0.08	-11.55 ± 0.09
NGC 4699	8.28 ± 0.05	2.28 ± 0.02	-0.64 ± 0.06	3.25 ± 0.18	2.20 ± 0.04	11.06 ± 0.08	-10.86 ± 0.09
NGC 4736	6.83 ± 0.10	2.03 ± 0.01	-0.64 ± 0.01	4.46 ± 0.10	2.71 ± 0.04	10.38 ± 0.08	-10.46 ± 0.09
NGC 4826	6.20 ± 0.11	1.99 ± 0.02	-0.38 ± 0.01	3.73 ± 0.11	2.21 ± 0.04	10.54 ± 0.08	-10.68 ± 0.09
NGC 4945	6.12 ± 0.30	2.07 ± 0.06	-0.80 ± 0.14	3.78 ± 0.07	3.56 ± 0.03	10.23 ± 0.08	-9.91 ± 0.09
NGC 7582	7.74 ± 0.18	2.07 ± 0.02	-0.32 ± 0.11	4.08 ± 0.17	3.29 ± 0.04	10.59 ± 0.08	-9.64 ± 0.09
UGC 3789	7.07 ± 0.04	2.03 ± 0.05	-0.24 ± 0.01	3.59 ± 0.13	3.22 ± 0.04	10.51 ± 0.08	-10.19 ± 0.09

**Table 1** *continued*

**Table 1** (*continued*)

Galaxy	$\log(M_\bullet)$	$\log(\sigma_0)$	$\log(R_e)$	$\log(\langle \Sigma_e \rangle)$	W2–W3	$\log(M^*)$	$\log(\text{sSFR})$
	[M <sub>⊙</sub> ]	[km s <sup>-1</sup> ]	[kpc]	[M <sub>⊙</sub> pc <sup>-2</sup> ]	[mag]	[M <sub>⊙</sub> ]	[yr <sup>-1</sup> ]
(1)	(2)	(3)	(4)	(5)	(6)	(7)	(8)

NOTE— **Column (1):** galaxy name. **Column (2):** black hole mass. **Column (3):** central stellar velocity dispersion. **Column (4):** equivalent-axis, effective (half-light) radius of the spheroid component. **Column (5):** average projected density within  $R_e$ . **Column (6):** WISE W2–W3 color. **Column (7):** galaxy stellar mass. **Column (8):** specific star-formation rate, i.e.,  $\log(\text{sSFR}) \equiv \log(\text{SFR}) - \log(M^*)$ .

576 As can be seen from the shape of the data in Figure 5, the data is predominantly characterized by linear relations  
577 and appears normally distributed in their logarithmic form, which underpins the general assumption for calculating  
578 BGe scores.<sup>13</sup>

### 579 C. EXACT POSTERIOR METHODOLOGY

580 We calculate the exact posteriors  $P(G | D)$  of the BGe scores for all DAGs from seven variables, separately for  
581 elliptical, lenticular, and spiral galaxies. The posterior probability of a graph given the data  $P(G | D)$  is proportional  
582 to the posterior probability of the data given a graph  $P(D | G)$  under a uniform prior, through Bayes' rule  $P(G | D) \propto$   
583  $P(D | G)P(G)$ . Under the assumption of linear and Gaussian data, the BGe score gives the marginal likelihood that  
584 the distribution of the data sample  $d = \{\mathbf{x}_1, \dots, \mathbf{x}_N\}$  of  $N$  variables is faithful (i.e., the data satisfies only and all the  
585 conditional independencies encoded by the DAG) to a hypothetical DAG model  $m^h$  as a product of local scores:

$$586 p(d |) = \prod_{i=1}^n \frac{p(d_i \cup \{X_i\} |)}{p(d^i |)}, \quad (\text{C1})$$

587 where  $i$  is the parent variables of the vertex  $i$ , and  $d^Y$  is the data restricted to the subset of data  $Y$ . The modularity  
588 (i.e., the full score is a product of local scores over all vertices  $i$ ) of local scores ensures that all DAGs in the same  
589 MEC are scored equally, and simplifies the posterior calculation over a large amount of DAGs. The local scores are  
590 further characterized by

$$591 p(d |) = \left( \frac{N}{N+} \right)^{l/2} \frac{\Gamma_l((N + -n + l)/2)}{\pi^{lN/2} \Gamma_l((-n + l)/2)} \frac{|T|^{(-n+l)/2}}{|R|^{(N+-n+l)/2}}. \quad (\text{C2})$$

592 The detailed explanation and full derivation of Equations C1 and C2 can be found in Kuipers et al. (2014). Empirically,  
593 many causal discovery methods based on the BGe score have been proven to successfully recover the ground truth  
594 causal structures in benchmark tests (Deleu et al. 2022; Emezue et al. 2023).

595 The steps of calculating exact posteriors can be summarized in the following steps:

- 596 1. Generate all possible DAGs for  $N$  variables represented by  $N \times N$  adjacency matrices  $A$ , with  $A_{i,j} = 1$  if there  
597 is an arrow from node  $i$  to node  $j$ .
- 598 2. For every DAG, generate its transitive closure represented by an adjacency matrix.
- 599 3. Calculate the posterior probability for every DAG given the data with the BGe score following Equation C1 (the  
600 sum of the scores over all DAGs is equal to unity by construction).
- 601 4. Perform a weighted average on all DAG adjacency matrices according to their posterior probabilities to get the  
602 matrix of edge marginals.

<sup>13</sup> The BGe score has also been shown to perform well in real-world scenarios where the data is not strictly linear and Gaussian, for example, in benchmark studies (Deleu et al. 2022; Emezue et al. 2023) using real flow cytometry data (Sachs et al. 2005), as well as simulated noisy data following an Erdős-Rényi model (Erdos & Renyi 1960).

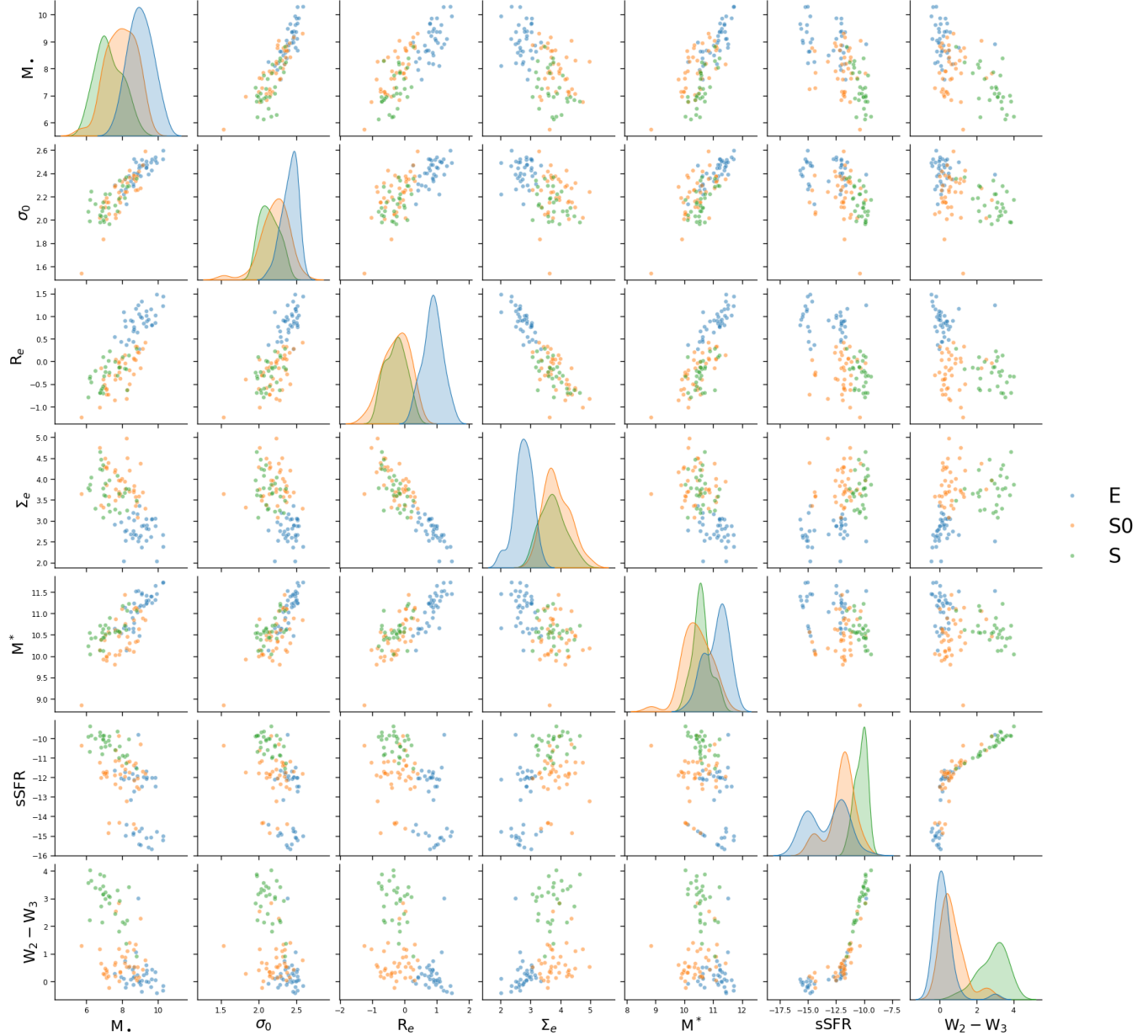


**Figure 5.** A pairplot of the data listed in Table 1.

603 5. Perform a weighted average on all transitive closure adjacency matrices according to their posterior probabilities  
604 to get the matrix of path marginals.

605 For a given value of  $N$ , steps 1 and 2 only need to be done once (i.e., the possible DAGs for  $N$  variables are unique),  
606 and only steps 3–5 need to be repeated for different datasets.

607 In this work, steps 2–5 are coded in a highly optimized and parallelized way on graphics processing units (GPUs),  
608 powered by a Python package JAX (Bradbury et al. 2018). The calculation of transitive closure adopts Warshall’s  
609 algorithm (Warshall 1962). The MECs for analysis are generated with a Python package causal-learn (Zheng et al.  
610 2023). The visualization of causal graphs is made possible through Python packages NetworkX (Hagberg et al. 2008)  
611 and PyGraphviz<sup>14</sup>.

<sup>14</sup> <https://pygraphviz.github.io/>

612

#### D. POSTERIOR DISTRIBUTION INSPECTION

613 In addition to Figure 1 (which shows the MEC with the highest posterior probability along with its corresponding  
 614 DAGs) and Figure 2 (which shows the edge and path marginals), here we take a deeper look at the posterior distribution.  
 615 Figure 6 shows the top four (in terms of posterior probabilities) MECs and Figure 7 shows the top ten DAGs. The top  
 616 graphs within each morphology class are similar to each other, and most of them convey the idea that elliptical galaxy  
 617 properties → SMBH mass, in spirals SMBH mass → galaxy properties, and lenticulars occupy the middle ground.  
 618 The paltry percentage of the total population for individual DAGs or MECs is not a rare and surprising phenomenon;  
 619 due to the huge space of possible causal structures, the number of possible DAGs grows *super-exponentially* as the  
 620 number of variables increases. The chance of drawing any DAG from a uniform distribution out of all possible DAGs  
 621 is  $8.781333053161975 \times 10^{-10}$ , which is  $\sim 10^6$  times smaller than the typical proportion around  $\sim 10^{-3}$  we observed for  
 622 the top DAGs (see Figure 7).

623 To better understand the relative posterior probability distribution and quantify the difference between graphs, in  
 624 Figure 8 we ordered DAGs and MECs by their posterior probabilities from highest to lowest. The posterior probability  
 625 is shown as solid lines and labeled on the left  $y$ -axis, and the rapidly dropping curves show that a few leading DAGs  
 626 and MECs are relatively much more probable than the DAGs and MECs in the long tail (note that the  $x$ -axis is in a  
 627 logarithmic scale). The dashed lines and the right  $y$ -axis show the *structural Hamming distance* (SHD), a standard  
 628 metric to evaluate the distance between graphs<sup>15</sup>, from each unique DAG or MEC to the most probable DAG or MEC.  
 629 From the SHDs, the top few DAGs or MECs are more similar to each other with fewer edges away from each other,  
 630 and less prominent DAGs or MECs are statistically more and more distinctive from the top ones. The SHD increases  
 631 the slowest in spirals, making the posterior distribution of spirals the most unimodal, while the SHD grows fastest  
 632 in lenticulars, reinforcing the picture that lenticulars, as the middle ground between ellipticals and spirals, have more  
 633 sub-modes of causal structures and no clear dominance of one particular causal direction between black hole mass  
 634 and galaxy properties. The probability distribution and SHD distribution together shows that despite the existence of  
 635 some sub-modes, a general mode of causal structure is detected in ellipticals and spirals respectively, and this general  
 636 mode can be visualized statistically via the edge marginals and path marginals in Figure 2, as discussed in §3. Finally,  
 637 we note that it is useful to remember for all interpretations of edge/path marginals that the null solution is nontrivial.  
 638 Indeed, there is not a 50–50 chance of one direction of causality or the other, but rather there are differing probabilities  
 639 of one direction, its reverse, or no direction of causality that vary depending on whether it is an edge or path marginal,  
 640 and it is not intuitive (see Figure 9)

641

#### E. SEMI-ANALYTICAL MODELS (SAMs)

642 As an additional benchmark test for the methodology under the SMBH–galaxy context, we practiced the same causal  
 643 discovery method on data generated by SAMs, where the ground truth causal direction is clearly defined, propagated  
 644 through a series of coupled partial-differential equations, and is easily customizable. The result of this test has been  
 645 presented in paragraphs related to Figure 3 in §4.2. Here we provide some details on the SAM dataset itself.

646 SAMs are powerful tools to model galaxy formation using dark matter halo merger trees from  $N$ -body simulations  
 647 with some phenomenological descriptions of baryonic physical processes like cosmic reionization, hot gas cooling and  
 648 cold gas infall, star formation and metal production, supernova feedback, gas stripping and tidal disruption of satellites,  
 649 galaxy mergers, bulge formation, black hole growth, AGNs feedback, etc. We adopt the model of Luo et al. (2016),  
 650 which is the resolution-independent version of the Munich galaxy formation model: L-Galaxies (mainly based on models  
 651 of Fu et al. 2013 and Guo et al. 2011, 2013). The dark matter only  $N$ -body simulation is the JiuTian-1G simulation  
 652 with  $6144^3$  dark matter particles in a  $1\text{ Gpc}/h$  cubic simulation box, based on Planck 2018 (Planck Collaboration  
 653 et al. 2020) cosmological parameters. In the model, there are two processes related to black hole growth and its  
 654 feedback. The first is “quasar mode” where SMBHs can accrete cold gas directly during galaxy mergers. The other  
 655 is “radio mode” where SMBHs can accrete hot gas continually from their host galaxies and inject energy into the  
 656 hot atmosphere. The quasar mode is the main black hole growth channel, while the radio mode is the main AGNs  
 657 feedback channel to suppress hot gas cooling. More details can be found in the supplementary material of Henriques  
 658 et al. (2015).

<sup>15</sup> SHD( $G, G^*$ ) counts the number of edges needed to add, delete, or revert, to move from one graph  $G$  to another graph  $G^*$ .

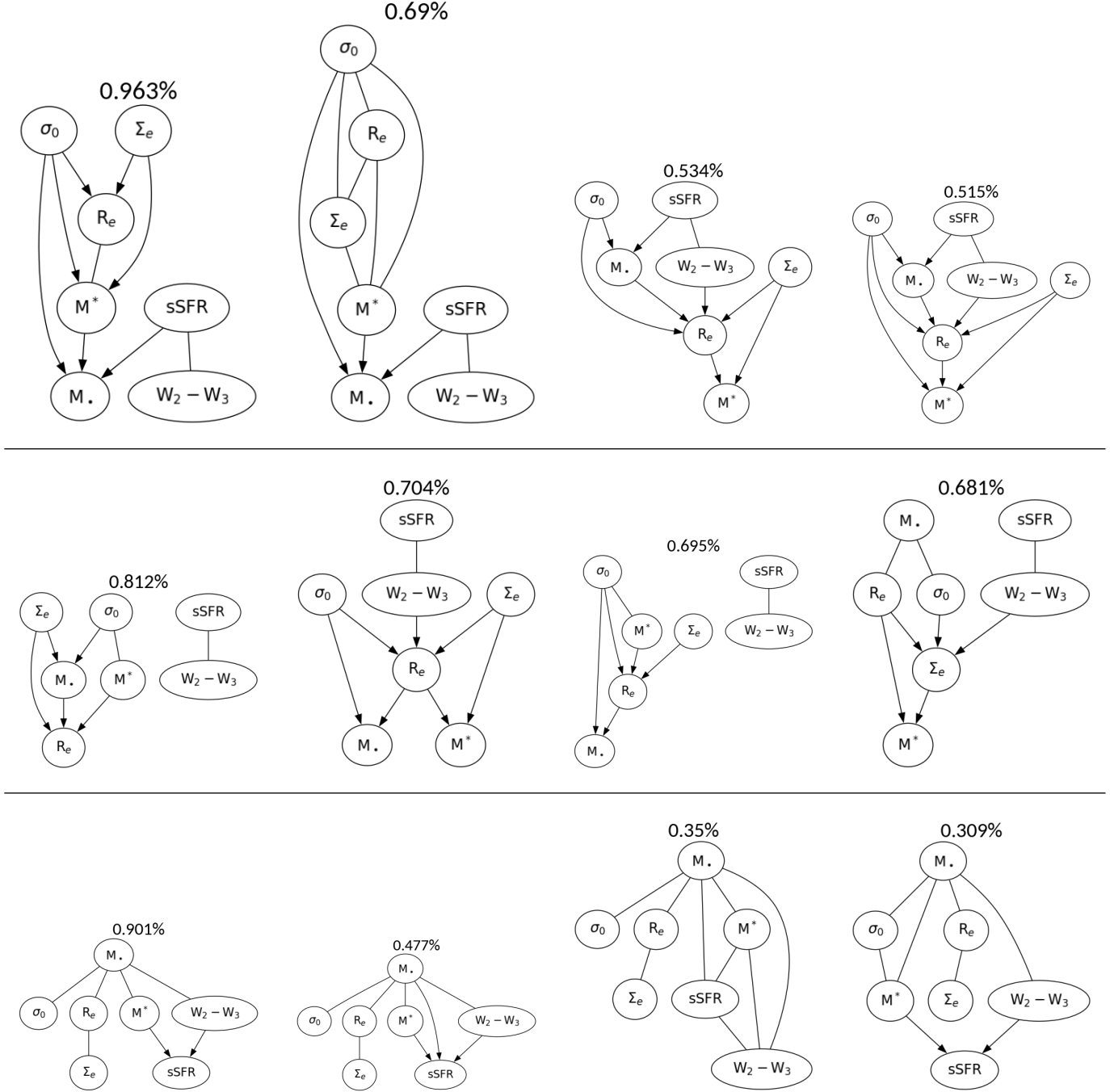


**Figure 6.** Exact posterior result for the top four Markov Equivalence Classes (MECs), represented as Partially Directed Acyclic Graphs (PDAGs) for *elliptical* (top panel), *lenticular* (middle panel), and *spiral* (bottom panel) galaxies. The posterior probability is labeled on top of each MEC, and is calculated by the sum of all DAG posterior probabilities within that MEC.

We use three groups of SAM galaxies: SAM E galaxies, SAM S galaxies, and SAM no-feedback galaxies. SAM E galaxies are galaxies with  $B/T > 0.78$  (bulge-to-total ratio,  $M_{\text{bulge}}^*/M^* > 0.78$  from Graham & Worley 2008), and SAM S galaxies are galaxies with  $B/T \leq 0.78$ . Additional stellar mass  $M^*$  cuts are applied such that the  $M^*$  distributions of SAM E and SAM S galaxies are similar to that of the real observational data used in this work for a fair comparison, as shown in Figure 10. No cuts are applied to SAM no-feedback galaxies since they do not have any realistic counterparts and are generated solely for this test. This gives us 1189 SAM E galaxies, 1999 SAM S galaxies, and 2663 SAM no-feedback galaxies.

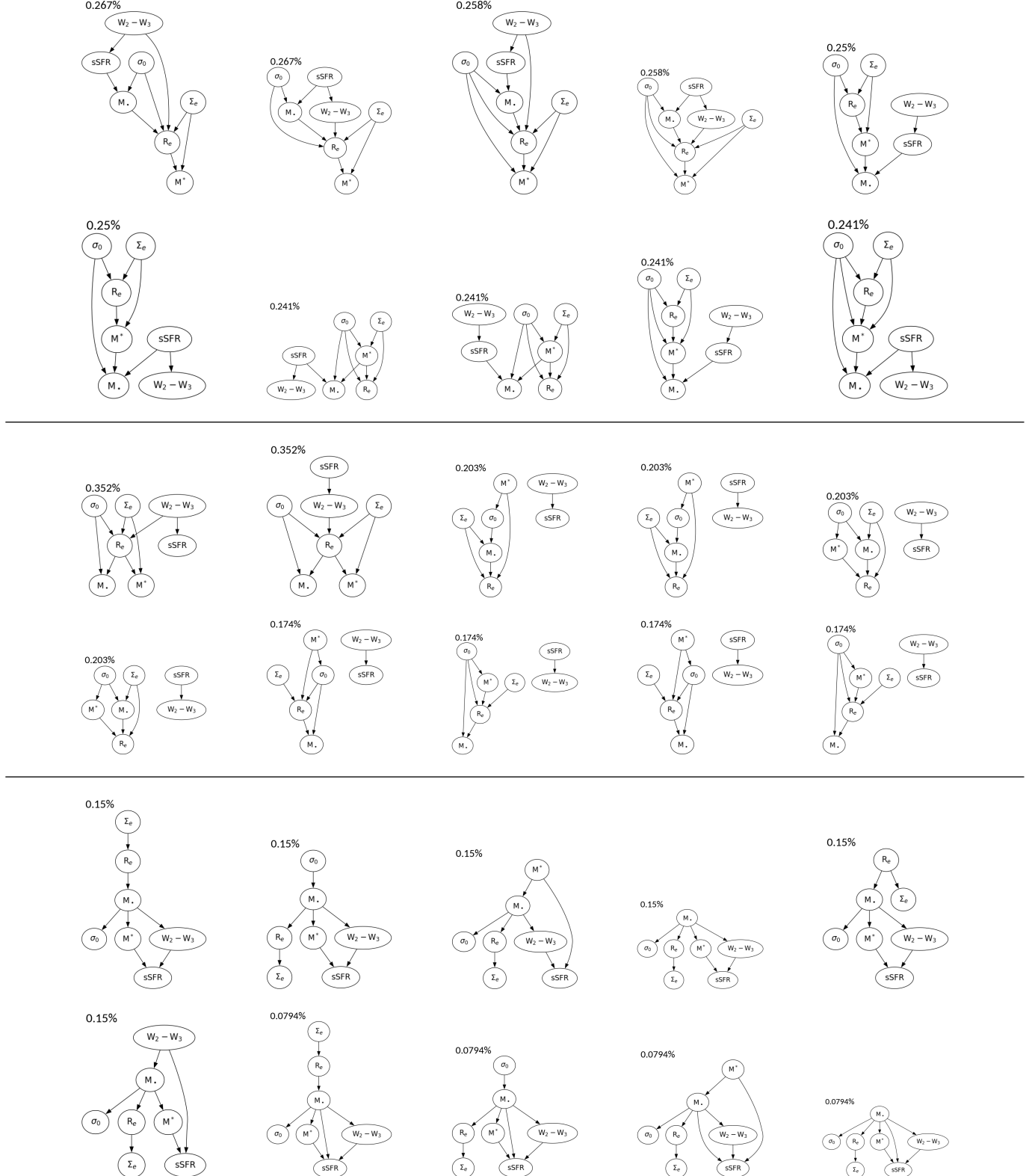


**Figure 7.** Exact posterior result for the top 10 most probable Directed Acyclic Graphs (DAGs) for *elliptical* (top panel), *lenticular* (middle panel), and *spiral* (bottom panel) galaxies. The percentage listed above each DAG indicates the posterior probability of the DAG, whereas the prior probability for every DAGs is equal to precisely  $8.781333053161975 \times 10^{-10}$  (OEIS Foundation Inc. 2024a).

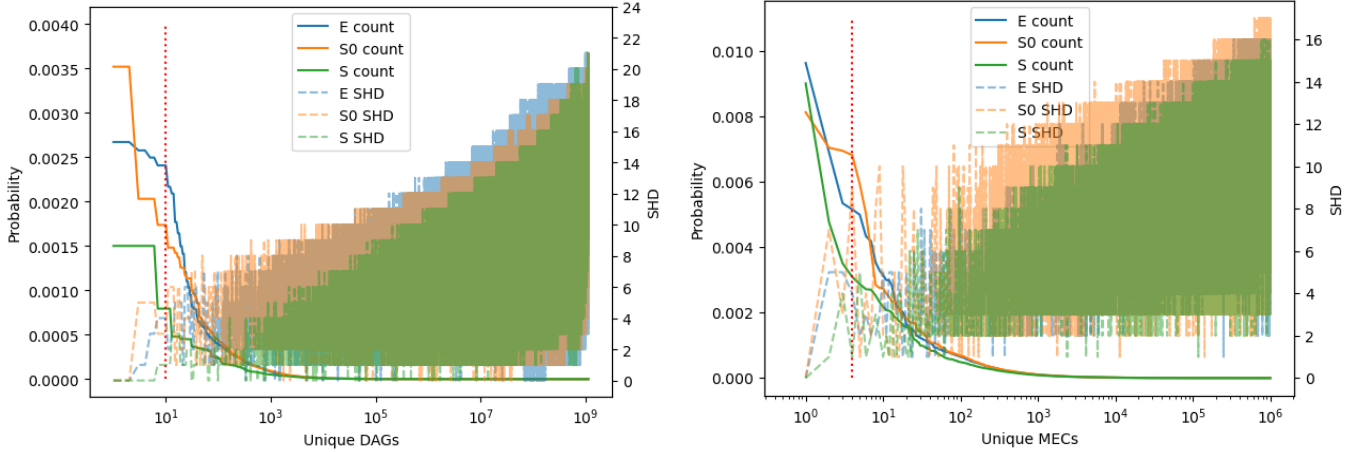


**Figure 8.** The exact posterior probability distribution and the structural Hamming distances (SHDs) to the most probable graph. There are in total  $3.12510571 \times 10^8$  MECs in the case of seven nodes (OEIS Foundation Inc. 2024b). Here, only the first  $10^6$  MECs are plotted for simplicity. The DAGs (left plot) and MECs (right plot) are ordered by their posterior probabilities from highest to lowest. The solid lines and the left  $y$ -axes show the posterior probability of the DAGs/MECs. The dashed lines and the right  $y$ -axes show the SHD, a measure of distance between graphs, from each DAG or MEC to the most probable DAG or MEC. The red dashed line marks the 10<sup>th</sup> DAG and the 4<sup>th</sup> MEC, which are shown in Figures 7 and 6, respectively.

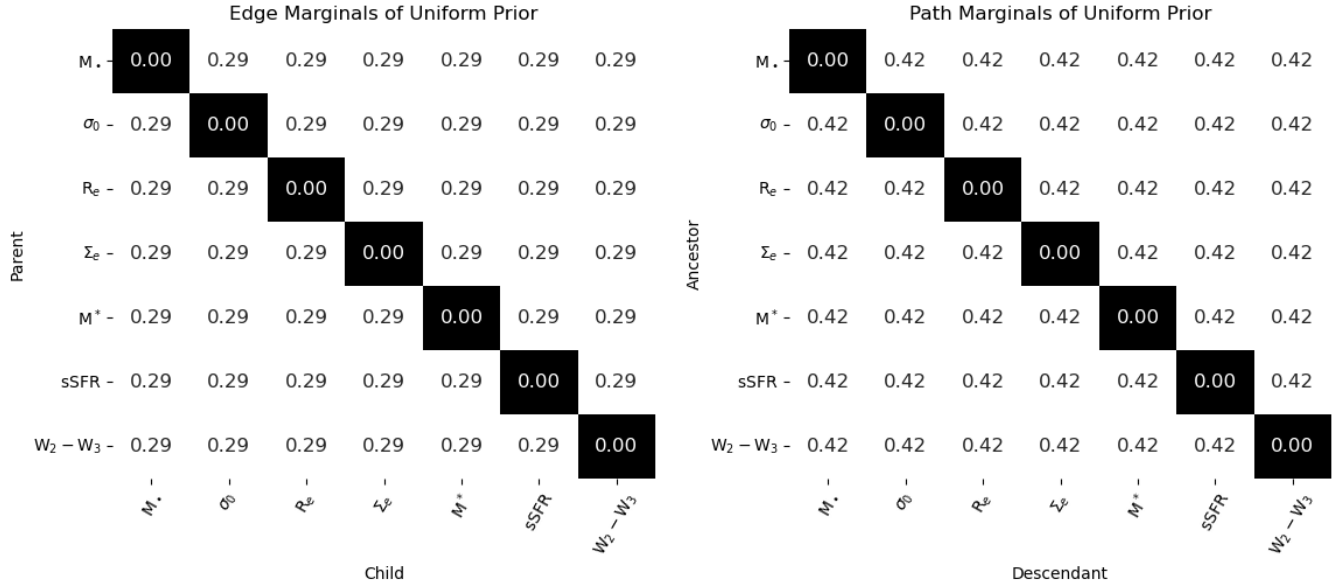


**Figure 9.** The *edge* marginals (left matrix) and *path* marginals (right matrix) for a uniform prior, i.e., all possible DAGs share the same probability.

## F. VERIFICATION WITH PC AND FCI

The PC and FCI algorithms, two *constraint-based methods* (in contrast with the *score-based method* adopted in this work), are also applied to the same observational data to cross-check our results. The details of these two time-tested algorithms are presented in §A.3.1. We adopt the implementation of PC and FCI in the Python package `causal-learn` (Zheng et al. 2023), and the results are reported in Figure 11. The exact posterior result including edge/path marginals (Figure 2) and the top MECs/DAGs (Figures 1, 6, and 7) are generally consistent with the causal graphs found by PC and FCI.

In ellipticals, the PC algorithm finds  $\sigma_0$  and sSFR cause  $M_\bullet$ . In our Bayesian approach,  $\sigma_0 \rightarrow M_\bullet$  and sSFR  $\rightarrow M_\bullet$  indeed have the highest and second highest edge/path marginals among the potential causes of  $M_\bullet$  in ellipticals.

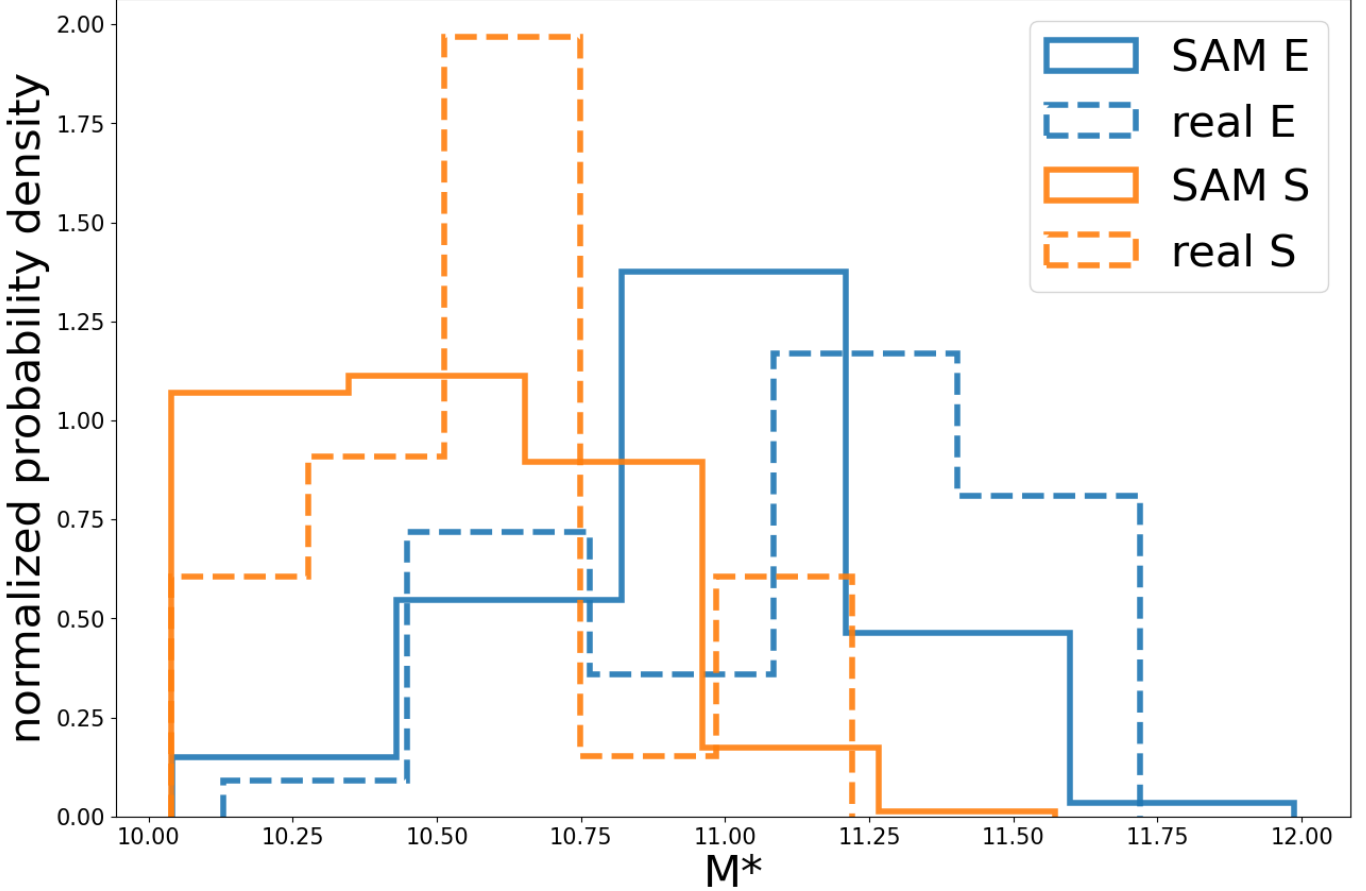


**Figure 10.** The  $M^*$  distribution for semi-analytical model (SAM) galaxies compared to the  $M^*$  distribution of real galaxies used in this work.

675 In spirals, the PC algorithm finds  $\sigma_0$ ,  $R_e$ , and  $M^*$  as effects of  $M_\bullet$ , and this is also consistent with the edge/path  
 676 marginals reported in our Bayesian approach. The FCI algorithm produces results compatible with those of the PC  
 677 algorithm, with the difference that, without the assumption of causal sufficiency, it leaves open the possibility that  
 678 all the relations between SMBH mass and its causal parents are confounded by unobserved variables. Particularly,  
 679 the double arrow between  $M_\bullet$  and sSFR in the lower left DAG of Figure 11 may indicate an unobserved confounder,  
 680 possibly the gas fraction, which in the future can be tested through hydrodynamical simulations where the gas fraction  
 681 is more accessible.

682 Note that here we adopt a relatively high value of  $\alpha = 0.15$ , the significance cutoff for the  $p$ -value of conditional  
 683 independence tests. Generally, a lower  $\alpha$  value gives more false negative errors (i.e., fails to identify causal relations  
 684 that exist), and a higher  $\alpha$  results in more false positive errors (i.e., identifies causal relations that do not exist).  
 685 Practically, the choice of  $\alpha$  is often empirical and highly depends on the context. Here in our case, the conditional  
 686 independence tests, which are the core of PC and FCI, suffer from the limited size of the dataset (35, 38, and 28 for  
 687 E, S0, and S galaxies, respectively). We therefore selected a higher value of  $\alpha$  to mitigate this. These limitations of  
 688 PC and FCI are one of the main motivations for our adoption of a Bayesian approach by relatively comparing the  
 689 posterior probabilities across all possible DAGs.

690

## G. POSSIBLE UNOBSERVED CONFOUNDERS

691 Our posterior calculation approach implicitly adopts the assumption of causal sufficiency, i.e., assuming there are  
 692 no unobserved confounders<sup>16</sup>. With the presence of an unobserved confounder, non-existing causal relations might be

<sup>16</sup> An unobserved confounder is a variable that is not included in the analysis but is a cause of two or more variables of interest.

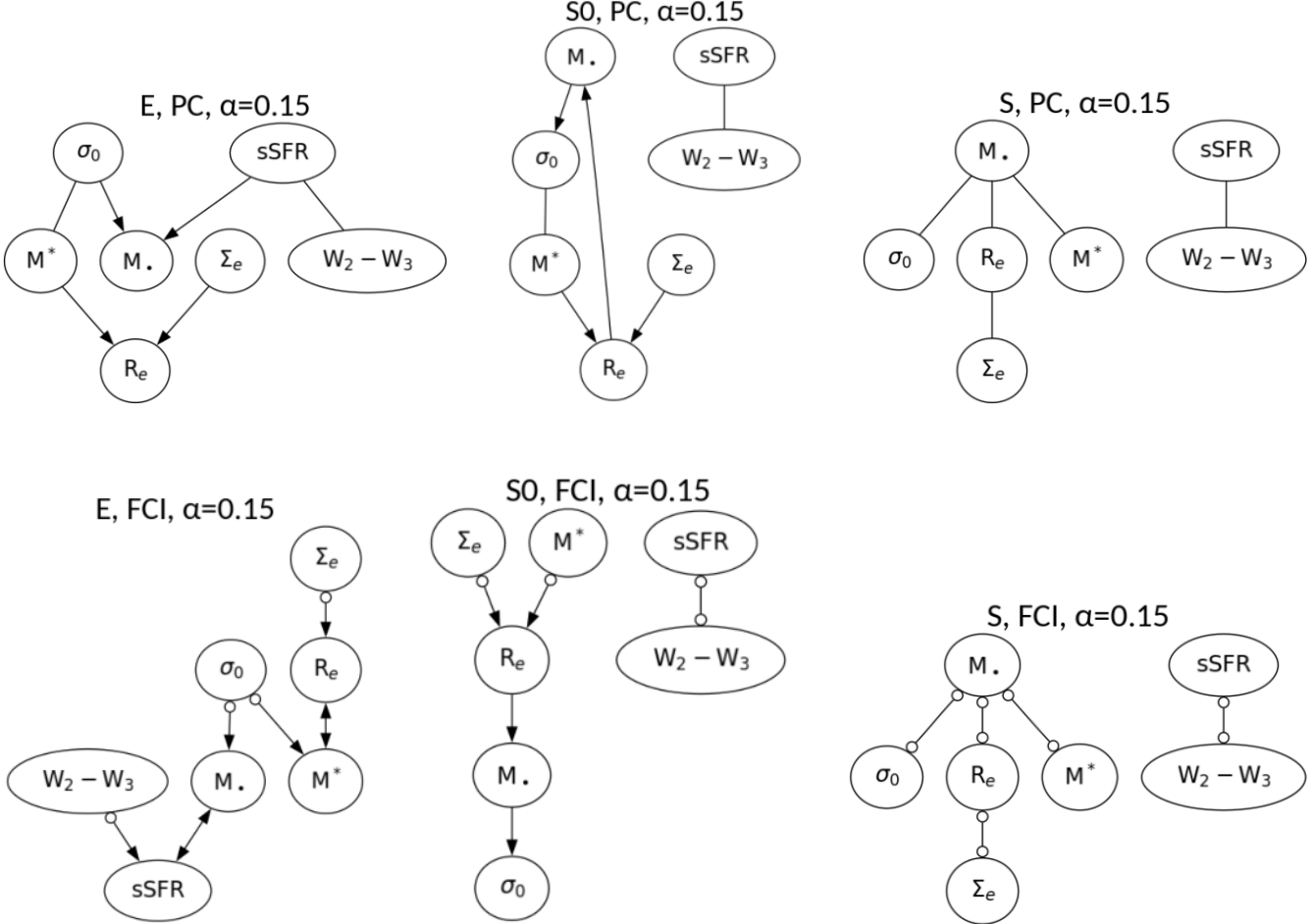


**Figure 11.** Graphs learned by the *PC* algorithm (*upper row*) and by the *FCI* algorithm (*bottom row*). The graphs in the *top row* use PDAGs to represent MECs of DAGs by leaving some edges undirected. The graphs in the *bottom row* are Partial Ancestral Graphs (PAGs) and introduce additional edge types:  $A \longleftrightarrow B$  corresponding to a confounding relation (i.e., a third variable causes both  $A$  and  $B$ ) and empty circles representing uncertainty regarding the ending symbol of the edge (i.e.,  $A \circ \rightarrow B$  may correspond to either  $A \rightarrow B$  or to  $A \longleftrightarrow B$ , but rules out  $B \rightarrow A$ ). The significance cutoff for conditional independence tests is set to  $\alpha = 0.15$  in all graphs.

693 falsely identified. Some potential unobserved confounders, such as the reserve of gas or merger history, are practically  
 694 difficult to observe but are already integrated into our interpretation. However, the distance from us to galaxies does  
 695 not directly play any role in galaxy formation theory nor in our interpretation, but might influence multiple variables  
 696 we examined, since our ability to measure all these seven variables decreases as distance increases and thus bias our  
 697 sample towards nearby and more massive BHs/galaxies. Therefore, we examined the impact of distance by performing  
 698 causal discovery with distance as one of the seven variables.

699 Since  $W2 - W3$  and  $sSFR$  are highly degenerate with each other, we replaced  $W2 - W3$  with  $D_L$ , the luminosity  
 700 distance to our targets<sup>17</sup>. The edge and path marginals with distance included are presented in Figure 12. Comparing  
 701 against the original marginals without distance (Figure 2), the presence of distance barely changes any previously  
 702 identified causal relations, since the edge and path marginals between galaxy properties and SMBH masses remains  
 703 unchanged with or without the inclusion of distance.

<sup>17</sup> Our luminosity distances are adopted from Graham & Sahu (2023b). Indeed, this sample of dynamically-measured black hole masses comes from galaxies that are all in the local Universe (median  $D_L = 19.3$  Mpc;  $z = 0.00439$  according to Planck Collaboration et al. 2020).

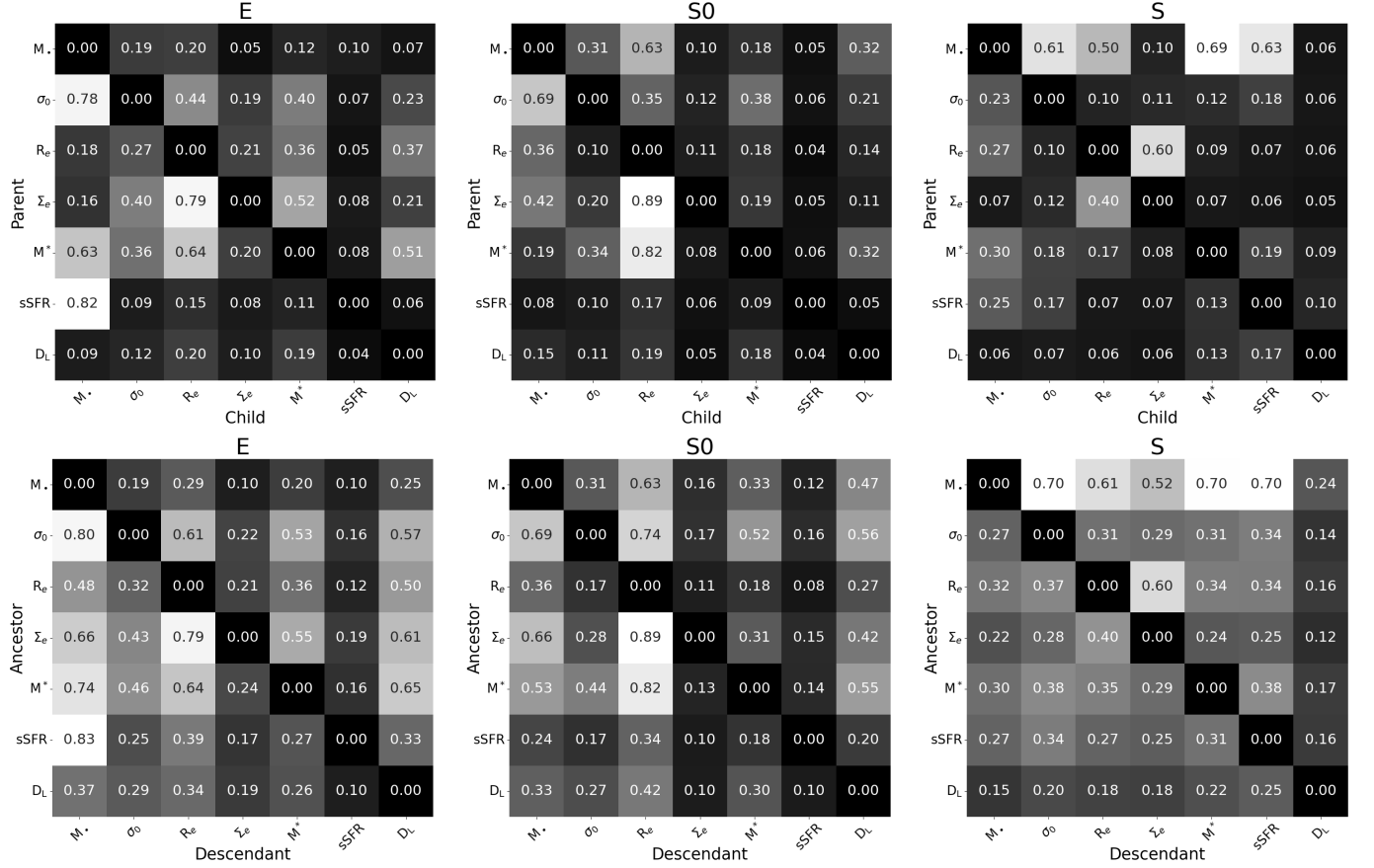


**Figure 12.** Edge marginals (top matrices) and path marginals (bottom matrices) with luminosity distance ( $D_L$ ) as one of the variables.

## H. STABILITY UNDER OBSERVATIONAL ERRORS

The variables used in this work are affected by observational errors and their marginal posterior probability distributions are given in Table 1 (assuming Gaussian posteriors). However, the causal structures explored so far have been calculated for the mean of these posteriors without considering their uncertainties. We now quantify the effect of this uncertainty on our inference of the causal structures. To do this, we draw samples from the posterior distribution of each variable to produce 100 mock datasets. The causal discovery method outlined in this paper is repeated on each of these 100 randomly-sampled datasets to arrive at 100 pairs of different edge marginal and path marginal matrices for each of the three morphological types considered. The edge marginal and path marginal matrices are summarized in Figure 13.

We find that, overall, the key findings of this study are robust against these uncertainties. For example, in ellipticals, the edge marginal between  $\sigma_0$  and  $M_*$  in both directions across random sampling realizations are  $0.70 \pm 0.09$  and  $0.26 \pm 0.07$ , giving a  $3.84\sigma$  discrepancy (in other words, the probability that the inferred direction of causality is due to noise and the resulting uncertainties in the variables is about  $10^{-4}$ ). Figure 14 shows the distribution of the edge marginals and path marginals for  $\sigma_0 \rightarrow M_*$ . The difference between ellipticals and spirals is evident for all realizations.

## I. STABILITY UNDER POSSIBLE OUTLIERS

We also explored the possibility of individual outlier galaxies biasing the inferred causal relations. To do this, we performed leave-one-out cross-validation. For ellipticals, lenticulars, and spirals, respectively, one galaxy is taken out at a time, and causal discovery is performed repeatedly (e.g., for 35 elliptical galaxies this procedure will be repeated 35 times). The mean and standard deviation of the resulting marginals are shown in Figure 15, and the marginals for  $\sigma_0 \rightarrow M_*$  are highlighted in Figure 16. As can be seen, the fluctuations due to leave-one-out are much smaller

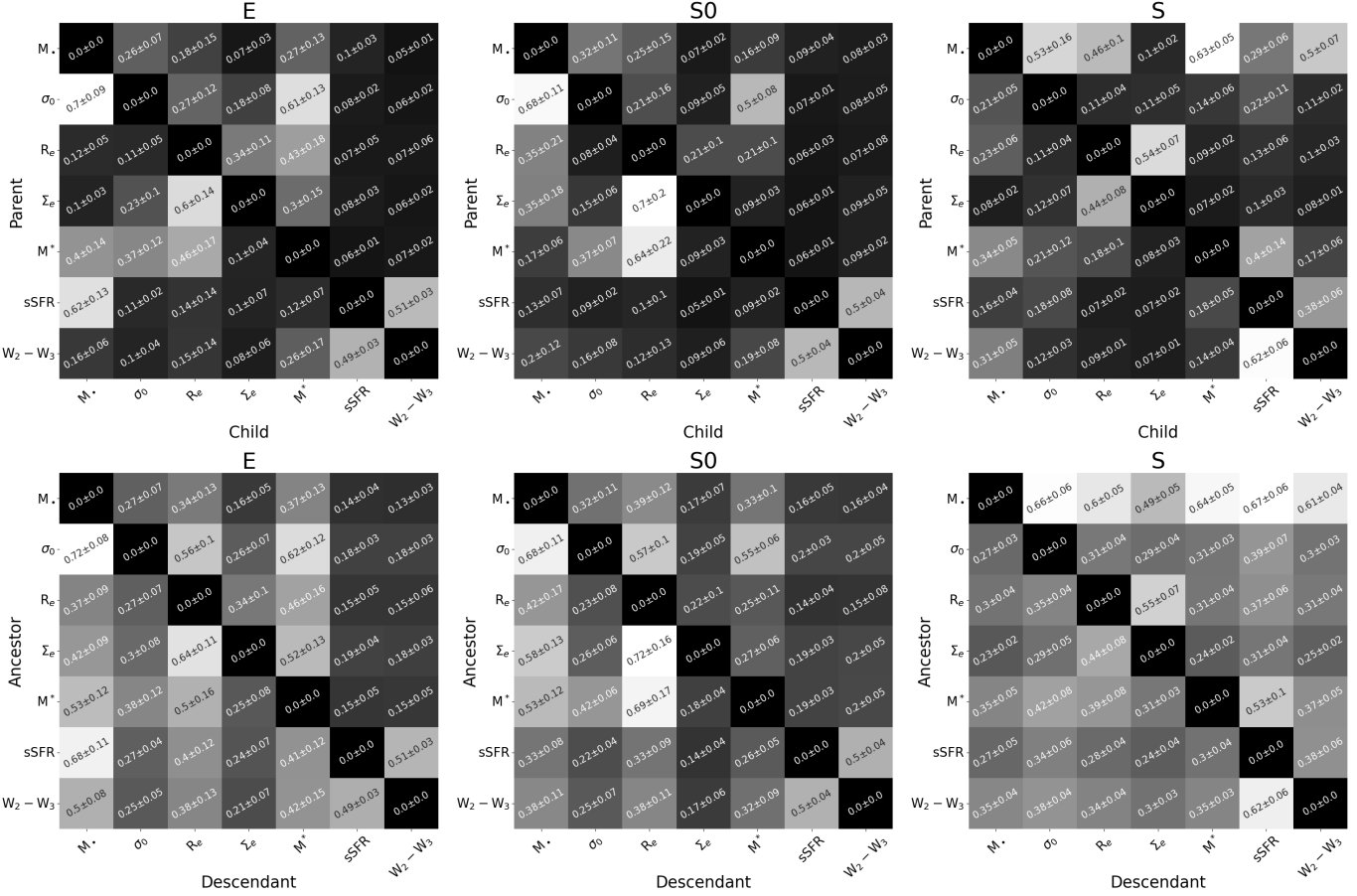


**Figure 13.** The mean and standard deviation of edge marginals (top matrices) and path marginals (bottom matrices) over 100 random sampling realizations for each morphological class.

724 than the uncertainties resulting from observational errors, suggesting that the results are not driven by any potential  
 725 individual outlier galaxy.

#### J. ESTIMATING POSTERIORS WITH DAG-GFN

726 The general timescale to perform the exact posterior search for seven variables outlined in this work, including  
 727 generating all possible DAGs, transitive closures, calculating posterior probabilities, and getting edge/path marginals,  
 728 is approximately a few hours. However, as the number of possible DAGs grows by a factor of  $\sim 10^2$  when the number of  
 729 variables increases from seven to eight, and by a factor of  $\sim 10^6$  when the number of variables increases from seven to  
 730 nine, an exact search becomes impractical. Here, we explore DAG-GFN as a feasible way to approximate the posteriors  
 731 as the number of variables increases.

732 The DAG-GFN method (Deleu et al. 2022) uses the framework of Generative Flow Networks (Bengio et al. 2021, 2023),  
 733 GFlowNets, to (approximately) sample from the posterior distribution. GFlowNets treat the problem of sampling from  
 734 an unnormalized distribution over discrete and compositional objects as a sequential decision-making problem, where  
 735 actions are taken by sampling from a learned policy at each step of generation. In the context of (Bayesian) causal  
 736 discovery, DAGs are constructed one edge at a time, starting from the empty graph. The objective is to find a policy  
 737  $\pi(G' | G)$  giving the probability of adding an edge to the DAG  $G$  to transform it into a new graph  $G'$ , such that  
 738 sampling sequentially from it would yield samples from a distribution proportional to  $R(G)$  (i.e., an unnormalized  
 739 distribution). Deleu et al. (2022) showed that such a policy satisfies

$$741 \frac{1}{|G|+1} R(G') \pi(\text{stop} | G) = R(G) \pi(G' | G) \pi(\text{stop} | G'), \quad (\text{J3})$$

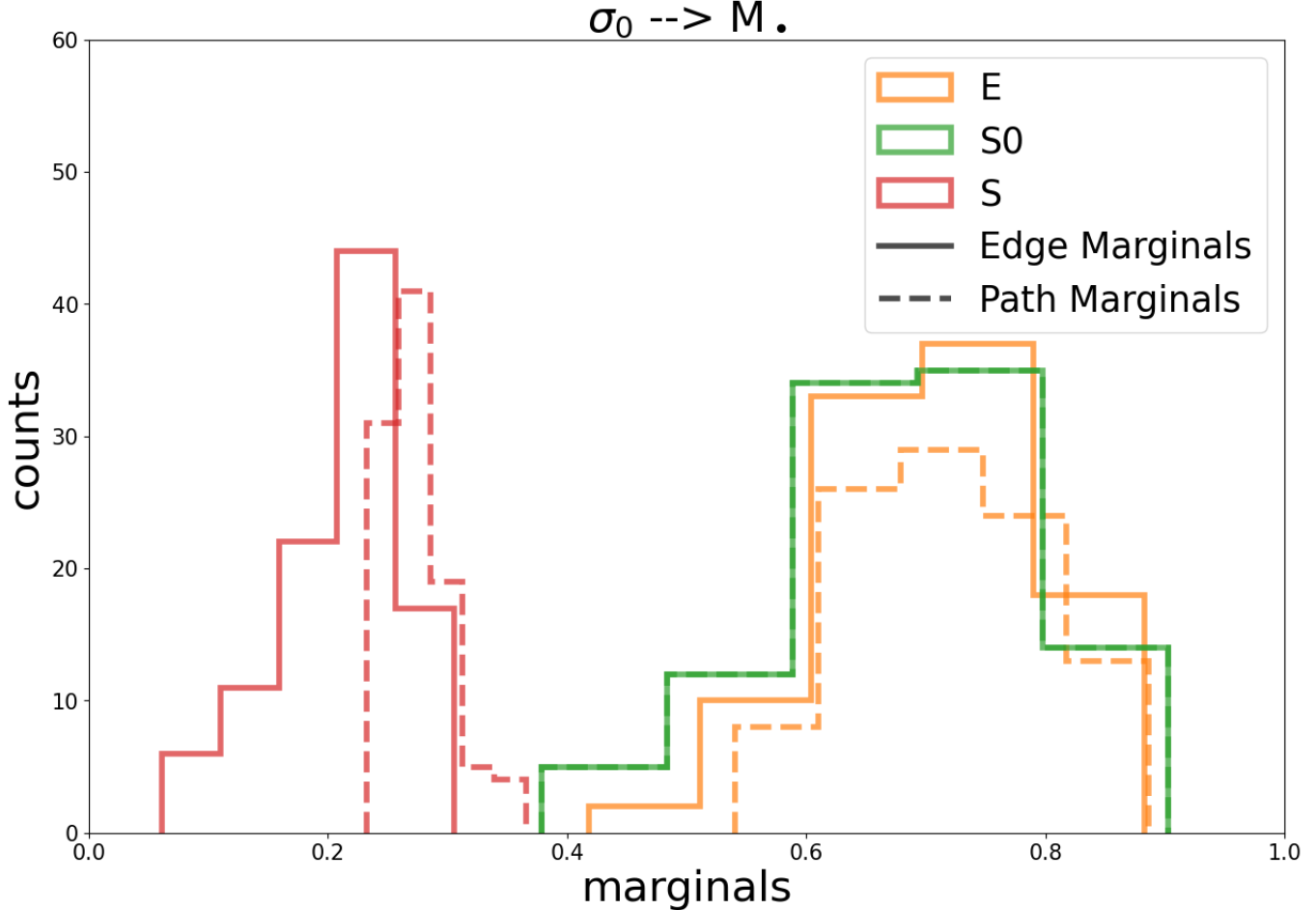


**Figure 14.** Edge marginal (—) and path marginal (---) distributions of  $\sigma_0 \rightarrow M_\bullet$  over 100 random realizations for each morphological class.

where  $|G|$  is the number of edges in  $G$ , and  $\pi(\text{stop} | G)$  is the probability of stopping the sequential process, effectively returning  $G$  as a sample of the posterior. To sample the posterior  $P(G | D) \propto P(D | G)P(G)$  (by Bayes' rule), we can then use  $R(G) = P(D | G)P(G)$ .

DAG-GFN was trained on our data, and  $10^5$  DAGs were sampled from the trained network. The frequency of each sampled unique DAG gives the approximated posterior probability of that DAG. The marginals, as well as the top MECs and DAGs are presented in Figures 17, 18, and 19, respectively. The approximated posteriors by DAG-GFN are highly consistent with the exact posteriors from our primary analysis. Visual inspection reveals that Figure 2 and Figure 17 present noticeable similarities.

750

## K. CYCLICITY

By calculating the posterior probabilities of all possible DAGs, we implicitly assumed acyclicity, i.e., no loops in a graph. In fact, the existence of feedback loops between black hole mass and galaxy properties (i.e., having black hole mass causing the galaxy properties, and then galaxy properties also causing black hole mass at the same time) is trivial in ellipticals and spirals according to galaxy formation theory. Black holes affect their host galaxies through black hole feedback, a process that heats the gas and pushes gas out to starve star formation, while galaxies also affect the central black hole through mergers and accretion. In an ideal spiral galaxy, there have been (at most) only minor mergers, thus killing off the merger path of galaxy  $\rightarrow$  black hole.

The accretion onto the black hole is mainly regulated by the black hole mass itself and the gas density in the central region (Bondi 1952). This latter quantity is found to be relatively constant in gas-rich galaxies, as confirmed by modern

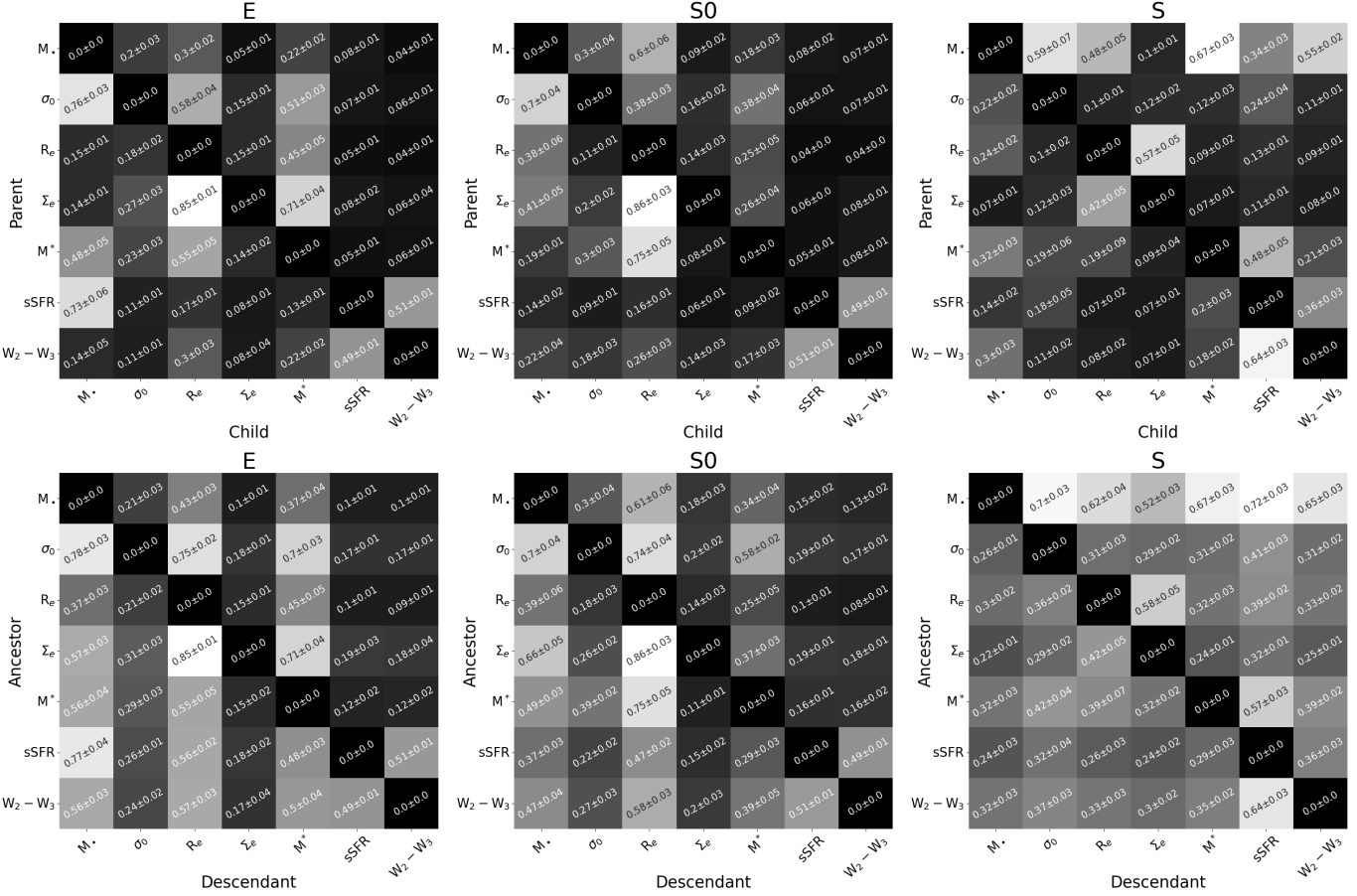


**Figure 15.** The mean and standard deviation of edge marginals (top matrices) and path marginals (bottom matrices) over all leave-one-out realizations.

numerical simulations, like the NIHAO suite (Wang et al. 2015; Blank et al. 2019) as shown in Figure 20. This implies that accretion is fairly constant in all gas-rich galaxies, diminishing the causal relation galaxy → black hole.

Therefore, in spiral galaxies, the causal relation of galaxy → black hole is expected to be very weak compared to the black hole → galaxy direction. On the other hand, ellipticals are in short supply of gas, therefore the central SMBH lacks the media in which to project its energy to regulate star formation. As a result, in ellipticals, the black hole → galaxy direction is negligible compared to the galaxy → black hole path enabled by major mergers.

In all (in spirals and ellipticals), one of the causal directions between SMBHs and galaxies is expected to considerably overwhelm the other, making the causal structure acyclic. The lenticulars, however, might have both major mergers and black hole feedback simultaneously, thus being more cyclic in their causal structure. This may be one of the reasons why we see many sub-modes in the posterior distributions of lenticulars as shown in Figure 8. To fully identify cyclic causal structures, time-series data is usually required. While in our case of SMBH–galaxy coevolution, which happens on a timescale of billions of years, obtaining time-series data is impossible within the lifetime of humanity<sup>18</sup>, studies of samples of galaxies with different ages may provide observational clues about the presence or absence of cyclicity in future studies.

<sup>18</sup> Except in simulations, which we will investigate in future work.

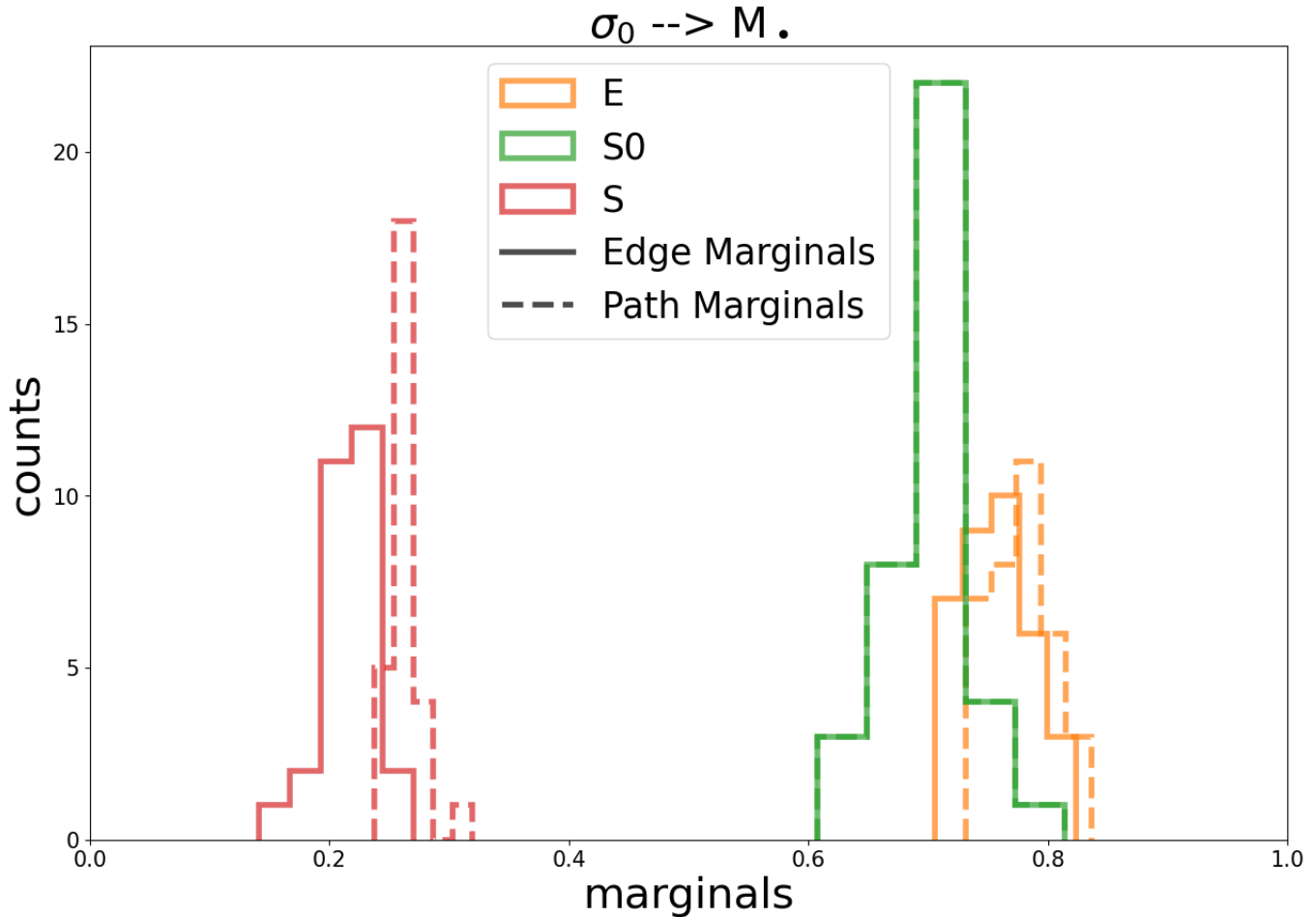


**Figure 16.** Edge marginal (—) and path marginal (---) distributions of  $\sigma_0 \rightarrow M_\bullet$  over all leave-one-out realizations.

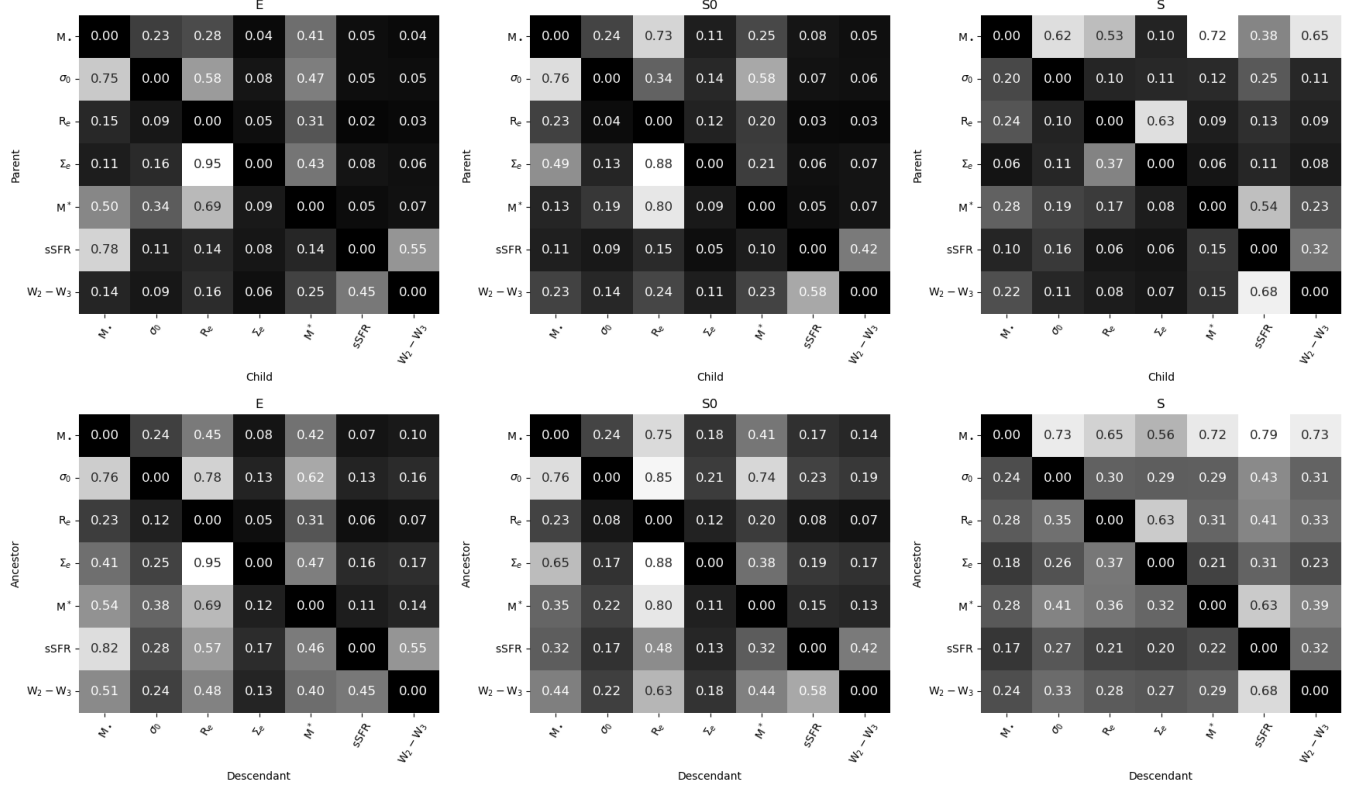


**Figure 17.** Edge marginals (top matrices) and path marginals (bottom matrices) approximated by DAG-GFN.

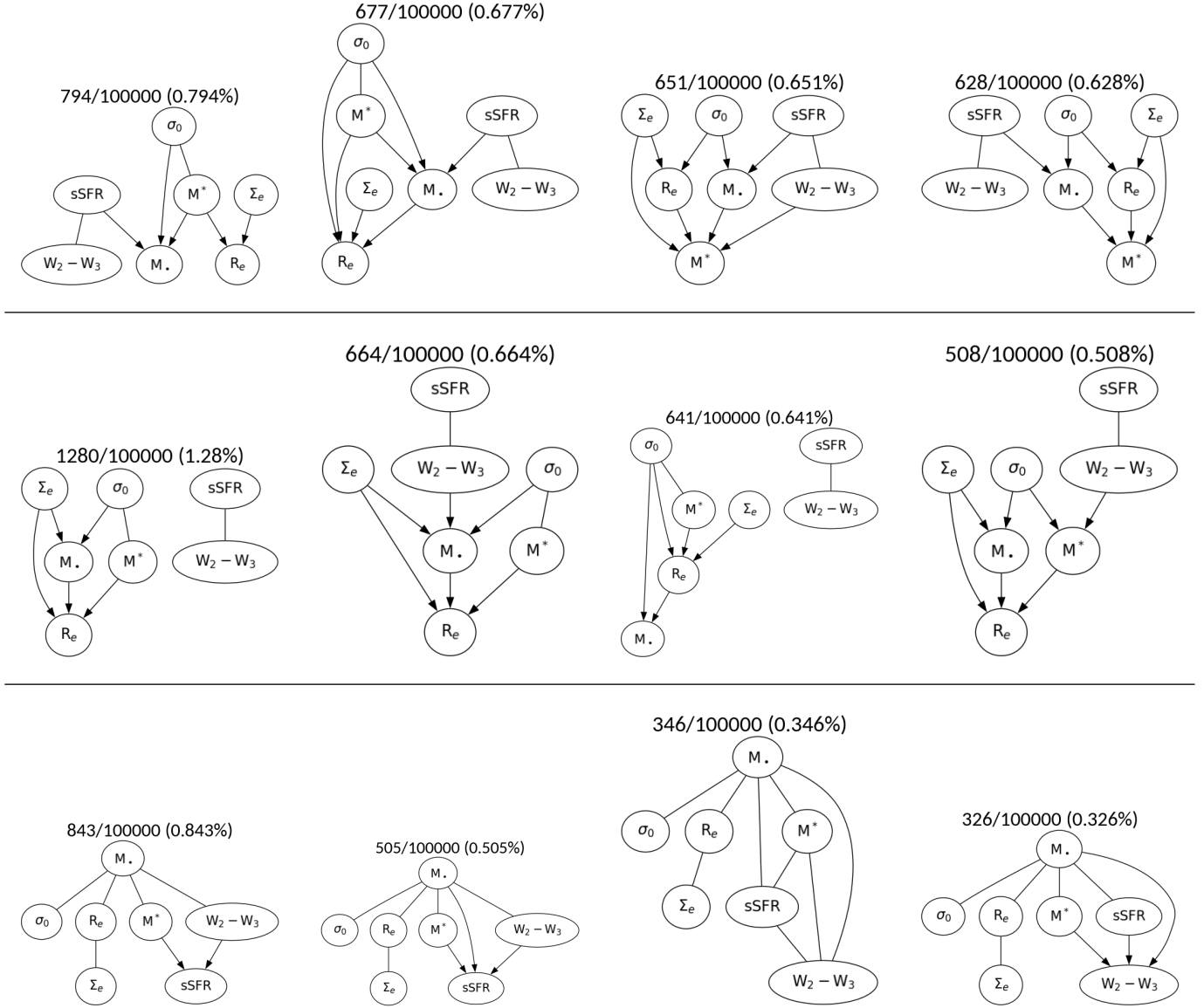


**Figure 18.** Top four MECs sampled by DAG-GFN for *elliptical* (top panel), *lenticular* (middle panel), and *spiral* (bottom panel) galaxies.

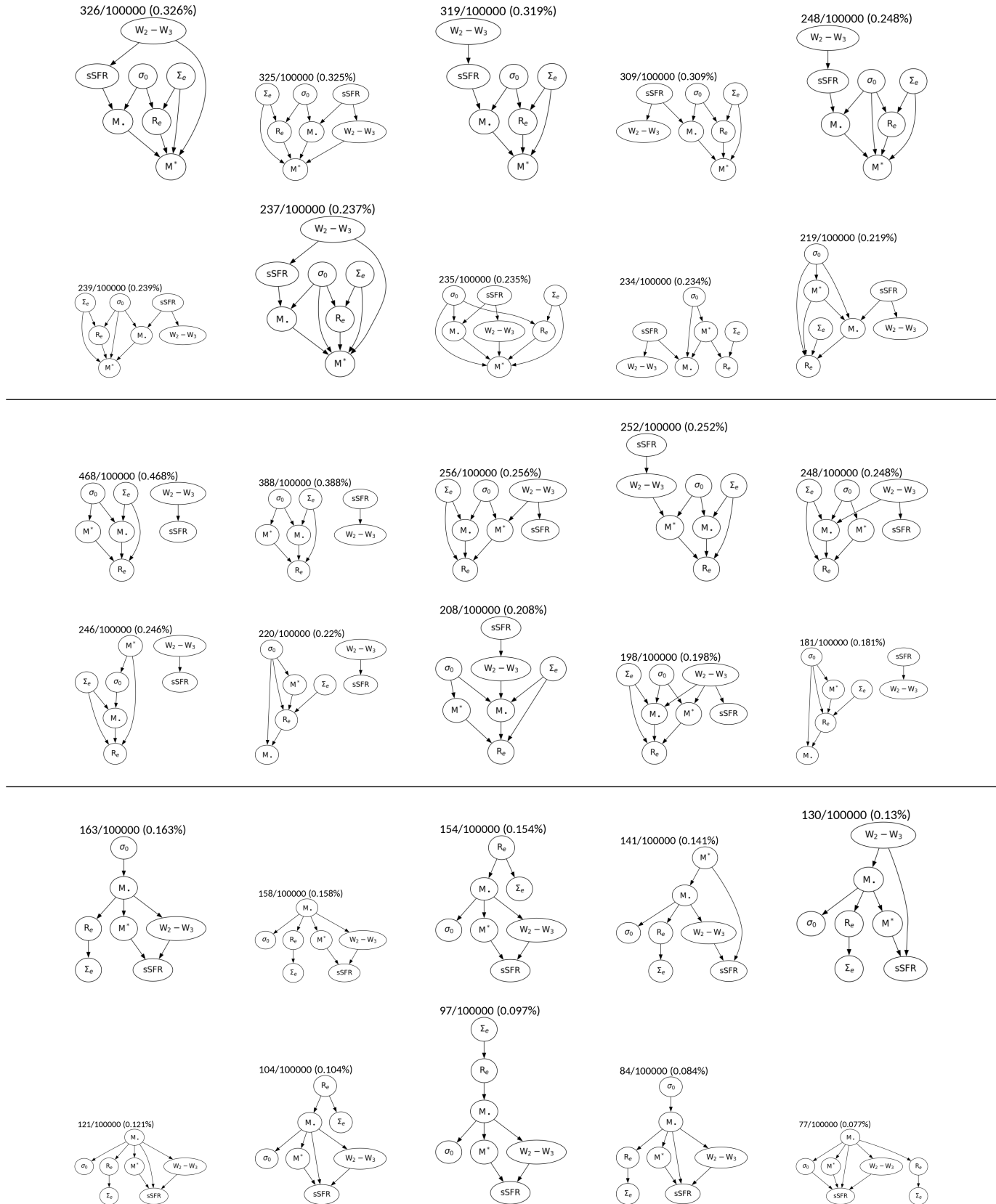


**Figure 19.** Top 10 DAGs sampled by DAG-GFN for *elliptical* (top panel), *lenticular* (middle panel), and *spiral* (bottom panel) galaxies.

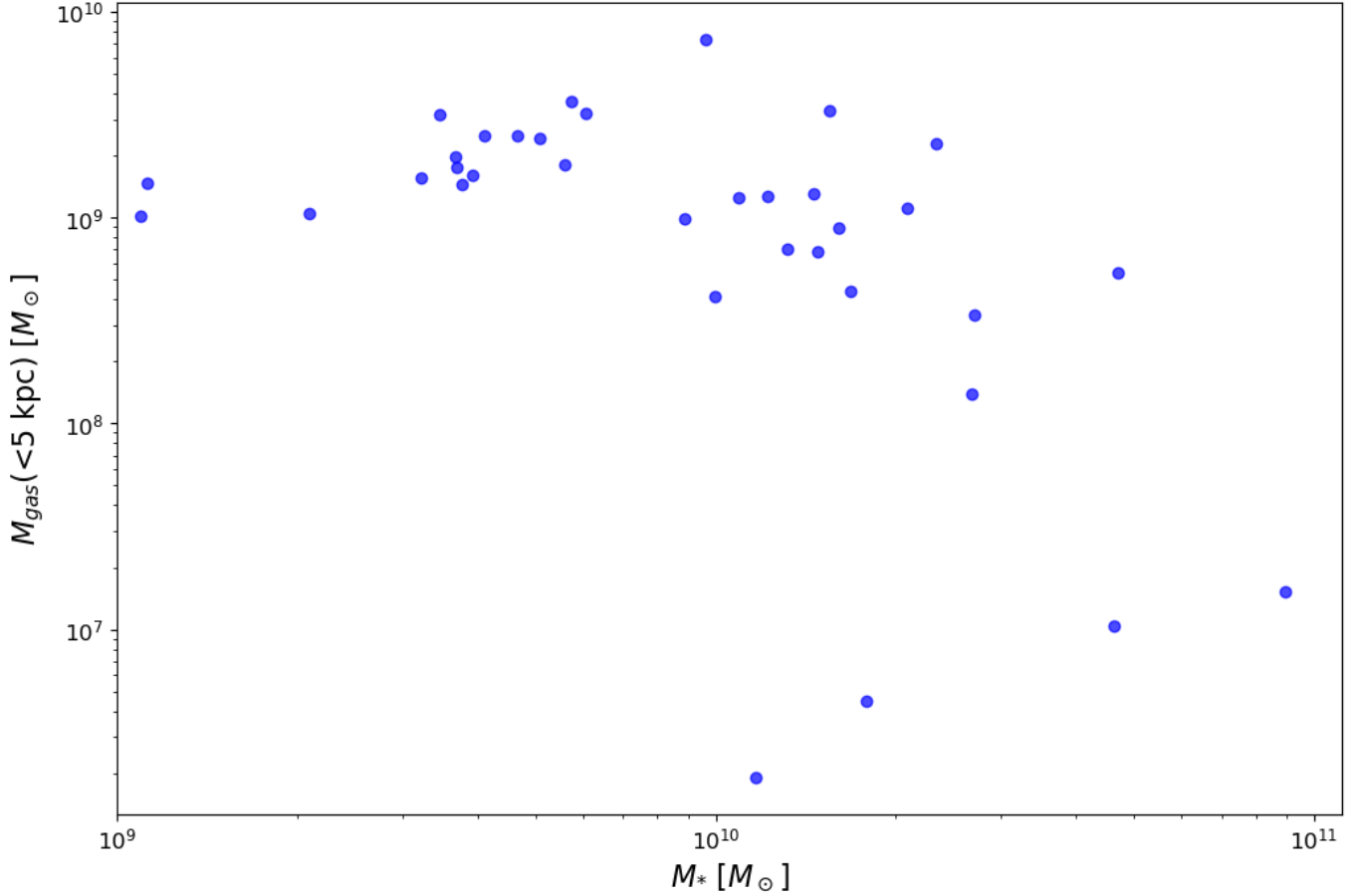


**Figure 20.** Gas mass within 5 kpc versus total stellar mass in NIHAO simulated galaxies (Wang et al. 2015). The central gas mass is fairly constant in gas rich galaxies, implying that gas accretion onto the black hole, which is mainly regulated by the black hole mass and the local gas density (Bondi 1952), is also quite uniform across galaxies, weakening the galaxy → SMBH causal relation in spirals.

## ORCID IDS

- 774 Zehao Jin (金泽灏) <https://orcid.org/0009-0000-2506-6645>
- 776 Mario Pasquato <https://orcid.org/0000-0003-3784-5245>
- 777 Benjamin L. Davis <https://orcid.org/0000-0002-4306-5950>
- 778 Tristan Deleu <https://orcid.org/0009-0005-1943-3484>
- 779 Yu Luo (罗煜) <https://orcid.org/0000-0003-2341-9755>
- 780 Changhyun Cho <https://orcid.org/0000-0002-9879-1749>
- 781 Pablo Lemos <https://orcid.org/0000-0002-4728-8473>
- 782 Laurence Perreault-Levasseur <https://orcid.org/0000-0003-3544-3939>
- 783 Yoshua Bengio <https://orcid.org/0000-0002-9322-3515>
- 784 Xi Kang (康熙) <https://orcid.org/0000-0002-5458-4254>
- 785 Andrea Valerio Macciò <https://orcid.org/0000-0002-8171-6507>
- 786 Yashar Hezaveh <https://orcid.org/0000-0002-8669-5733>

## REFERENCES

- 787 Ahmed, O., Tr'uble, F., Goyal, A., et al. 2020,  
788 CausalWorld: A Robotic Manipulation Benchmark for  
789 Causal Structure and Transfer Learning
- 790 Allahverdyan, A. E., & Janzing, D. 2008, *Journal of  
791 Statistical Mechanics: Theory and Experiment*, 2008,  
792 04001
- 793 Allen, J.-M. A., Barrett, J., Horsman, D. C., Lee, C. M., &  
794 Spekkens, R. W. 2017, *Phys. Rev. X*, 7, 031021
- 795 Ankan, A., & Panda, A. 2015, in Proceedings of the 14th  
796 Python in Science Conference (SCIPY 2015), Citeseer
- 797 Bengio, E., Jain, M., Korablyov, M., Precup, D., & Bengio,  
798 Y. 2021, Advances in Neural Information Processing  
799 Systems (NeurIPS)
- 800 Bengio, Y., Deleu, T., Hu, E. J., et al. 2023, Journal of  
801 Machine Learning Research (JMLR)
- 802 Blank, M., Macciò, A. V., Dutton, A. A., & Obreja, A.  
803 2019, *MNRAS*, 487, 5476
- 804 Bluck, A. F. L., Maiolino, R., Brownson, S., et al. 2022,  
805 *A&A*, 659, A160
- 806 Bondi, H. 1952, *MNRAS*, 112, 195
- 807 Bradbury, J., Frostig, R., Hawkins, P., et al. 2018, JAX:  
808 composable transformations of Python+NumPy  
809 programs, 0.3.13. <http://github.com/google/jax>
- 810 Brockman, G., Cheung, V., Pettersson, L., et al. 2016,  
811 OpenAI Gym
- 812 Cannarozzo, C., Leauthaud, A., Oyarzún, G. A., et al.  
813 2023, *MNRAS*, 520, 5651
- 814 Catelan, M., Ferraro, F. R., & Rood, R. T. 2001, *ApJ*, 560,  
815 970
- 816 Cheng, A. F., Rivkin, A. S., Michel, P., et al. 2018,  
817 *Planet. Space Sci.*, 157, 104
- 818 Chickering, D. 2002, *Journal of Machine Learning  
819 Research*, 3, 507-554
- 820 Cluver, M. E., Jarrett, T. H., Dale, D. A., et al. 2017, *ApJ*,  
821 850, 68
- 822 Davis, B., & Jin, Z. 2024, in American Astronomical  
823 Society Meeting Abstracts, Vol. 56, American  
824 Astronomical Society Meeting Abstracts, 152.06
- 825 Davis, B. L., Graham, A. W., & Cameron, E. 2018, *ApJ*,  
826 869, 113
- 827 —. 2019a, *ApJ*, 873, 85
- 828 Davis, B. L., Graham, A. W., & Combes, F. 2019b, *ApJ*,  
829 877, 64
- 830 Davis, B. L., Graham, A. W., & Seigar, M. S. 2017,  
831 *MNRAS*, 471, 2187
- 832 Davis, B. L., & Jin, Z. 2023, *ApJL*, 956, L22
- 833 Deleu, T., Góis, A., Emezue, C., et al. 2022, Conference on  
834 Uncertainty in Artificial Intelligence (UAI)
- 835 Di Capua, G., Runge, J., Donner, R. V., et al. 2020,  
836 *Weather and Climate Dynamics*, 1, 519
- 837 Di Matteo, T., Colberg, J., Springel, V., Hernquist, L., &  
838 Sijacki, D. 2008, *ApJ*, 676, 33
- 839 Di Matteo, T., Springel, V., & Hernquist, L. 2005, *Nature*,  
840 433, 604
- 841 Djorgovski, S., & Davis, M. 1987, *ApJ*, 313, 59
- 842 Ellison, S. L., Viswanathan, A., Patton, D. R., et al. 2019,  
843 *MNRAS*, 487, 2491
- 844 Emezue, C. C., Drouin, A., Deleu, T., Bauer, S., & Bengio,  
845 Y. 2023, in ICML 2023 Workshop on Structured  
846 Probabilistic Inference & Generative Modeling.  
847 <https://openreview.net/forum?id=9aDnWNPyeC>
- 848 Erdos, P., & Renyi, A. 1960, Publications of the  
849 Mathematical Institute of the Hungarian Academy of  
850 Sciences, 5, 17-61
- 851 Falcón-Barroso, J., Peletier, R. F., & Balcells, M. 2002,  
852 *MNRAS*, 335, 741

- 853 Ferrarese, L., & Merritt, D. 2000, *ApJL*, 539, L9  
 854 Fu, J., Kauffmann, G., Huang, M.-l., et al. 2013, *MNRAS*,  
 855 434, 1531  
 856 Gaspari, M., Ruszkowski, M., & Oh, S. P. 2013, *MNRAS*,  
 857 432, 3401  
 858 Gebhard, T. D., Bonse, M. J., Quanz, S. P., & Schölkopf,  
 859 B. 2022, *A&A*, 666, A9  
 860 Gebhardt, K., Bender, R., Bower, G., et al. 2000, *ApJL*,  
 861 539, L13  
 862 Geiger, D., & Heckerman, D. 1994, in Proceedings of the  
 863 Tenth International Conference on Uncertainty in  
 864 Artificial Intelligence, UAI'94 (San Francisco, CA, USA:  
 865 Morgan Kaufmann Publishers Inc.), 235–243  
 866 Geiger, D., & Heckerman, D. 2002, *Ann. Statist.*, 30,  
 867 1412–1440  
 868 Graham, A. W. 2019, *MNRAS*, 487, 4995  
 869 —. 2023a, *MNRAS*, 521, 1023  
 870 —. 2023b, *MNRAS*, 518, 6293  
 871 —. 2024, *MNRAS*, 531, 230  
 872 Graham, A. W., Jarrett, T. H., & Cluver, M. E. 2024,  
 873 *MNRAS*, 527, 10059  
 874 Graham, A. W., & Sahu, N. 2023a, *MNRAS*, 520, 1975  
 875 —. 2023b, *MNRAS*, 518, 2177  
 876 Graham, A. W., & Scott, N. 2013, *ApJ*, 764, 151  
 877 Graham, A. W., & Worley, C. C. 2008, *MNRAS*, 388, 1708  
 878 Greenwood, E. 1945, Experimental sociology: A study in  
 879 method (Columbia University Press)  
 880 Guo, Q., White, S., Angulo, R. E., et al. 2013, *MNRAS*,  
 881 428, 1351  
 882 Guo, Q., White, S., Boylan-Kolchin, M., et al. 2011,  
 883 *MNRAS*, 413, 101  
 884 Hagberg, A. A., Schult, D. A., & Swart, P. J. 2008, in  
 885 Proceedings of the 7th Python in Science Conference, ed.  
 886 G. Varoquaux, T. Vaught, & J. Millman, Pasadena, CA  
 887 USA, 11 – 15  
 888 Harris, C. R., Millman, K. J., van der Walt, S. J., et al.  
 889 2020, *Nature*, 585, 357–362  
 890 Heckerman, D., Geiger, D., & Chickering, D. 1995, *Machine  
 891 Learning*, 20, 197–243  
 892 Heckman, T. M., & Best, P. N. 2014, *ARA&A*, 52, 589  
 893 Henriques, B. M. B., White, S. D. M., Thomas, P. A., et al.  
 894 2015, *MNRAS*, 451, 2663  
 895 Huang, B., Zhang, K., Lin, Y., Schölkopf, B., & Glymour,  
 896 C. 2018, in Proceedings of the 24th ACM SIGKDD  
 897 International Conference on Knowledge Discovery &  
 898 Data Mining, KDD '18 (New York, NY, USA:  
 899 Association for Computing Machinery), 1551–1560.  
 900 <https://doi.org/10.1145/3219819.3220104>  
 901 Hubble, E. P. 1936, Realm of the Nebulae  
 902 Hunter, J. D. 2007, *Computing in Science & Engineering*, 9,  
 903 90–95  
 904 Imbens, G. W., & Lemieux, T. 2008, *Journal of  
 905 econometrics*, 142, 615–635  
 906 Jahnke, K., & Macciò, A. V. 2011, *ApJ*, 734, 92  
 907 Janzing, D. 2007, *arXiv e-prints*, arXiv:0708.3411  
 908 Jarrett, T. H., Cluver, M. E., Taylor, E. N., et al. 2023,  
 909 *ApJ*, 946, 95  
 910 Jeans, J. H. 1928, *Astronomy and cosmogony*  
 911 Kalainathan, D., Goudet, O., & Dutta, R. 2020, *Journal of  
 912 Machine Learning Research*, 21, 1–5  
 913 Kormendy, J., & Ho, L. C. 2013, *ARA&A*, 51, 511  
 914 Kuipers, J., Moffa, G., & Heckerman, D. 2014, *arXiv  
 915 e-prints*, arXiv:1402.6863  
 916 Larson, R. L., Finkelstein, S. L., Kocevski, D. D., et al.  
 917 2023, *ApJL*, 953, L29  
 918 Leifer, M. S., & Spekkens, R. W. 2013, *PhRvA*, 88, 052130  
 919 Luo, Y., Kang, X., Kauffmann, G., & Fu, J. 2016, *MNRAS*,  
 920 458, 366  
 921 M. Mooij, J., & Claassen, T. 2020, in Proceedings of  
 922 Machine Learning Research, Vol. 124, Proceedings of the  
 923 36th Conference on Uncertainty in Artificial Intelligence  
 924 (UAI), ed. J. Peters & D. Sontag (PMLR), 1159–1168.  
 925 <https://proceedings.mlr.press/v124/m-mooij20a.html>  
 926 Madigan, D., York, J., & Allard, D. 1995, *International  
 927 Statistical Review / Revue Internationale de Statistique*,  
 928 63, 215–232  
 929 Magorrian, J., Tremaine, S., Richstone, D., et al. 1998, *AJ*,  
 930 115, 2285  
 931 Makarov, D., Prugniel, P., Terekhova, N., Courtois, H., &  
 932 Vauglin, I. 2014, *A&A*, 570, A13  
 933 Marinacci, F., Vogelsberger, M., Pakmor, R., et al. 2018,  
 934 *MNRAS*, 480, 5113  
 935 McKinney, W. 2010, in Proceedings of the 9th Python in  
 936 Science Conference, Vol. 445, Austin, TX, 51–56  
 937 Menegozzo, G., Dall'Alba, D., & Fiorini, P. 2022, in 2022  
 938 IEEE 18th International Conference on Automation  
 939 Science and Engineering (CASE), 2124–2131  
 940 Mould, J. 2020, *Frontiers in Astronomy and Space Sciences*,  
 941 7, 21  
 942 Naiman, J. P., Pillepich, A., Springel, V., et al. 2018,  
 943 *MNRAS*, 477, 1206  
 944 Nelson, D., Pillepich, A., Springel, V., et al. 2018, *MNRAS*,  
 945 475, 624  
 946 OEIS Foundation Inc. 2024a, Number of acyclic digraphs  
 947 (or DAGs) with n labeled nodes, Entry A003024 in The  
 948 On-Line Encyclopedia of Integer Sequences.  
 949 <https://oeis.org/A003024>

- 950 —. 2024b, Number of essential graphs with n nodes (in 1-1  
 951 correspondence with Markov equivalence classes of  
 952 acyclic digraphs). <https://oeis.org/A007984>
- 953 Ostriker, J. P., Spitzer, Lyman, J., & Chevalier, R. A. 1972,  
 954 *ApJL*, 176, L51
- 955 Pang, X., Yu, Z., Tang, S.-Y., et al. 2021, *ApJ*, 923, 20
- 956 Pasquato, M., Jin, Z., Lemos, P., Davis, B. L., & Macciò,  
 957 A. V. 2023, arXiv e-prints, arXiv:2311.15160
- 958 Pasquato, M., & Matsiuk, N. 2019, *Research Notes of the  
 959 American Astronomical Society*, 3, 179
- 960 Pearl, J. 2009, Causality (Cambridge university press)
- 961 Pearl, J., Glymour, M., & Jewell, N. P. 2016, Causal  
 962 inference in statistics : a primer (Chichester, West  
 963 Sussex: Wiley)
- 964 Pillepich, A., Nelson, D., Hernquist, L., et al. 2018,  
 965 *MNRAS*, 475, 648
- 966 Planck Collaboration, Aghanim, N., Akrami, Y., et al.  
 967 2020, *A&A*, 641, A6
- 968 Rodriguez-Gomez, V., Genel, S., Vogelsberger, M., et al.  
 969 2015, *MNRAS*, 449, 49
- 970 Rodriguez-Gomez, V., Pillepich, A., Sales, L. V., et al.  
 971 2016, *MNRAS*, 458, 2371
- 972 Runge, J., Bathiany, S., Boltt, E., et al. 2019, *Nature  
 973 communications*, 10, 2553
- 974 Sachs, K., Perez, O., Pe'er, D., Lauffenburger, D. A., &  
 975 Nolan, G. P. 2005, *Science*, 308, 523-529
- 976 Sahu, N., Graham, A. W., & Davis, B. L. 2019a, *ApJ*, 876,  
 977 155
- 978 —. 2019b, *ApJ*, 887, 10
- 979 —. 2020, *ApJ*, 903, 97
- 980 Savorgnan, G., Graham, A. W., Marconi, A., et al. 2013,  
 981 *MNRAS*, 434, 387
- 982 Savorgnan, G. A. D., & Graham, A. W. 2016, *ApJS*, 222, 10
- 983 Savorgnan, G. A. D., Graham, A. W., Marconi, A., & Sani,  
 984 E. 2016, *ApJ*, 817, 21
- 985 Schaye, J., Dalla Vecchia, C., Booth, C. M., et al. 2010,  
 986 *MNRAS*, 402, 1536
- 987 Schölkopf, B., Hogg, D. W., Wang, D., et al. 2016,  
 988 *Proceedings of the National Academy of Science*, 113,  
 989 7391
- 990 Scott, N., Graham, A. W., & Schombert, J. 2013, *ApJ*, 768,  
 991 76
- 992 Scutari, M. 2014
- 993 Sijacki, D., Springel, V., Di Matteo, T., & Hernquist, L.  
 994 2007, *MNRAS*, 380, 877
- 995 Silk, J., & Rees, M. J. 1998, *A&A*, 331, L1
- 996 Soliman, N. H., Macciò, A. V., & Blank, M. 2023, *MNRAS*,  
 997 525, 12
- 998 Spekkens, R. 2023, Causal Inference Lecture - 230306,  
 999 Perimeter Institute. <https://pirsa.org/23030069>
- 1000 Spirtes, P. 2001, in Proceedings of Machine Learning  
 1001 Research, Vol. R3, Proceedings of the Eighth  
 1002 International Workshop on Artificial Intelligence and  
 1003 Statistics, ed. T. S. Richardson & T. S. Jaakkola  
 1004 (PMLR), 278–285.  
<https://proceedings.mlr.press/r3/spirtes01a.html>
- 1005 Spirtes, P., Glymour, C. N., & Scheines, R. 2000,  
 1006 Causation, prediction, and search (MIT press)
- 1007 Springel, V., White, S. D. M., Jenkins, A., et al. 2005,  
 1008 *Nature*, 435, 629
- 1009 Springel, V., Pakmor, R., Pillepich, A., et al. 2018,  
 1010 *MNRAS*, 475, 676
- 1011 Van Rossum, G., & Drake, F. L. 2009, Python 3 Reference  
 1012 Manual (Scotts Valley, CA: CreateSpace)
- 1013 Viinikka, J., Hyttinen, A., Pensar, J., & Koivisto, M. 2020,  
 1014 in Advances in Neural Information Processing Systems,  
 1015 ed. H. Larochelle, M. Ranzato, R. Hadsell, M. Balcan, &  
 1016 H. Lin, Vol. 33 (Curran Associates, Inc.), 6584–6594.  
[https://proceedings.neurips.cc/paper\\_files/paper/2020/file/48f7d3043bc03e6c48a6f0ebc0f258a8-Paper.pdf](https://proceedings.neurips.cc/paper_files/paper/2020/file/48f7d3043bc03e6c48a6f0ebc0f258a8-Paper.pdf)
- 1017 Virtanen, P., Gommers, R., Oliphant, T. E., et al. 2020,  
 1018 *Nature Methods*, 17, 261
- 1019 Vowels, M. J., Camgoz, N. C., & Bowden, R. 2022, *ACM  
 1020 Comput. Surv.*, 55
- 1021 Wang, L., Dutton, A. A., Stinson, G. S., et al. 2015,  
 1022 *MNRAS*, 454, 83
- 1023 Warshall, S. 1962, *J. ACM*, 9, 11–12
- 1024 Waskom, M. L. 2021, *Journal of Open Source Software*, 6,  
 1025 3021
- 1026 Waterval, S., Macciò, A. V., Buck, T., et al. 2024, *MNRAS*,  
 1027 533, 1463
- 1028 Wood, C. J., & Spekkens, R. W. 2015, *New Journal of  
 1029 Physics*, 17, 033002
- 1030 Wright, E. L., Eisenhardt, P. R. M., Mainzer, A. K., et al.  
 1031 2010, *AJ*, 140, 1868
- 1032 Zheng, Y., Huang, B., Chen, W., et al. 2023, arXiv e-prints,  
 1033 arXiv:2307.16405